

We are IntechOpen, the world's leading publisher of Open Access books Built by scientists, for scientists

6,900

Open access books available

186,000

International authors and editors

200M

Downloads

Our authors are among the

154

Countries delivered to

TOP 1%

most cited scientists

12.2%

Contributors from top 500 universities



WEB OF SCIENCE™

Selection of our books indexed in the Book Citation Index
in Web of Science™ Core Collection (BKCI)

Interested in publishing with us?
Contact book.department@intechopen.com

Numbers displayed above are based on latest data collected.
For more information visit www.intechopen.com



Application of TiO₂ Nanotubes Gas Sensors in Online Monitoring of SF₆ Insulated Equipment

Ju Tang, Xiaoxing Zhang, Song Xiao and Fuping Zeng

Additional information is available at the end of the chapter

<http://dx.doi.org/10.5772/intechopen.68328>

Abstract

Titanium dioxide nanotube arrays (TNTAs) are a typical three-dimensional nanomaterial. TNTA has rich chemical and physical properties and low manufacturing costs. Thus, TNTA has broad application prospects. In recent years, research has shown that because of its large specific surface area and nanosize effect, the TNTAs have an enormous potential for development compared with other nanostructure forms in fields such as light catalysis, sensor, and solar batteries. TNTAs have become the hotspot of international nanometer material research. The tiny gas sensor made from TNTA has several advantages, such as fast response, high sensitivity, and small size. Several scholars in this field have achieved significant progress. As a sensitive material, TNTA is used to test O₂, NO₂, H₂, ethanol, and other gases. In this chapter, three SF₆ decomposed gases, namely SO₂, SOF₂ and SO₂F₂, are chosen as probe gases because they are the main by-products in the decomposition of SF₆ under PD. Then, the adsorption behaviors of these gases on different anatase (101) surfaces including intrinsic, Pt-doped and Au-doped, are studied using the first principles density functional theory (DFT) calculations. The simulation results can be used as supplement for gas-sensing experiments of TNTA gas sensors. This work is expected to add insights into the fundamental understanding of interactions between gases and TNTA surfaces for better sensor design.

Keywords: SF₆ decomposed gas, anatase TiO₂ surface, metal doping, adsorption, sensing mechanism, density functional theory

1. Introduction of titanium nanotubes

TiO₂ nanotubes are typically one-dimensional material, which has a wealth of physical and chemical properties and low production cost, and therefore, it bears a broad application

prospects [1, 2]. In particular, recent studies show that, due to large specific surface area and nanosize effect, compared with other forms of nanostructures, TiO₂ nanotubes show great potential for development in photocatalysis, sensors, solar cells and other areas [1, 3, 10]. It has become the research focus of nanomaterials internationally [1, 4–9]. The particular photocatalytic properties of TiO₂ under UV irradiation can degrade pollutants and reduce desorption time, thus extending the lifetime of sensors that based on TiO₂, which provides more opportunity for the development of high-quality new sensors.

1.1. Properties of titanium nanotubes

TiO₂ is one common type of N semiconductor oxide, of which the outer electron distribution is 3d²4s². The molecular structure of TiO₂ belongs to flash zinc crystal lattice. Its structural center, Ti atom, is surrounded by six oxygen atoms, forming an octahedral structure which coordination number is 6. TiO₂ outer layer of 3d electronics is not active and 4 valence electrons of it form a covalent bond with O atom. From the above, we can know that the chemical properties of TiO₂ are very stable. It cannot dissolve in most acid, such as hydrochloric acid, nitric acid and dilute sulfuric acid, except concentrated sulfuric acid and hydrofluoric acid. The band gap of TiO₂ is approximately 3.2 eV. Its electrical conductivity is extremely low at room temperature. Even at high temperature, it only has a small conductivity. So its resistance is very big. We can almost see TiO₂ as an insulator. TiO₂'s conductance is achieved by activating the exciting electrons on the additional energy level to the conduction band. The additional level can be introduced from defects and impurities in TiO₂. So the types and quantities of these defects and impurities determine the TiO₂ conductivity type. Therefore, some methods may be employed to form a certain type of defect and impurity level or defect levels in the band gap to change the conductive properties of TiO₂.

There are three TiO₂ polymorphs in nature: rutile, anatase and brookite. Anatase and rutile structures are most widely used. Although rutile and anatase TiO₂ crystalline belong to the same tetragonal, but they have two different lattices. And thus, the X-ray images are different.

Anatase TiO₂ XRD diffraction angle 2θ is located in 25.5°, and rutile TiO₂ XRD diffraction angle 2θ is located in 27.5°. Rutile TiO₂ crystal forms a titanium atom in the lattice center, surrounded by six oxygen atoms which are located in octahedral edges and corners, and a cell composed of two moleculars is the most stable crystal structure. Anatase TiO₂ crystal form is composed of four TiO₂ molecules in a crystal cell, which is stable at low temperature. When the temperature reaches 610°C, it gradually transforms into rutile, and its transformation accelerated rapidly at 730°C, and it can transform into rutile completely at 915°C. Plate titanium ore TiO₂ crystal form, belonging to orthorhombic system, is a cell composed of six TiO₂ moleculars, which is an unstable crystal form that transforms into rutile type when the temperature is higher than 650°C. **Figure 1** is the schematic diagram for the three kinds of morphology of crystalline structure of TiO₂.

Plate titanium ore crystal form belongs to the metastable phase, and thus its structure is unstable, which is therefore rarely used in industrial production. Anatase and rutile belong to the same crystal system, but the atomic arrangement of rutile is compact, so its relative density as

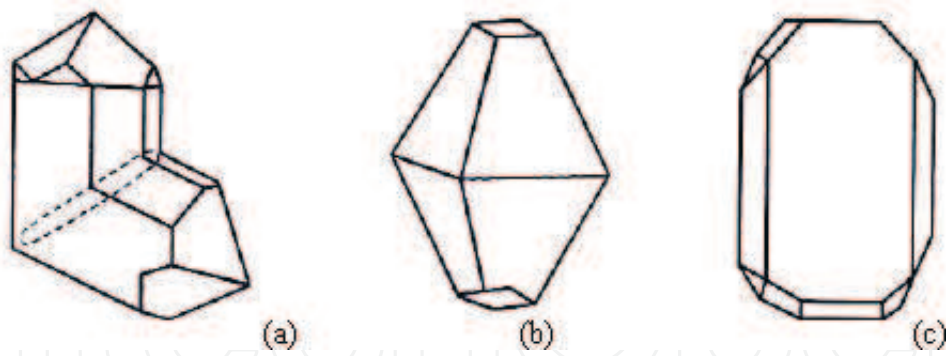


Figure 1. Morphology of crystalline structure of TiO₂ (a) rutile (b) anatase (c) brookite.

well as refractive index is larger, and it has very good properties of scattered light, as well as the shielding effect to UV light, while anatase, with good photocatalytic activity, has a wide application prospect in the aspects of environmental protection and electrochemical sensor.

1.2. Preparation method of titanium nanotubes

Currently, there are three types of the method for preparing TiO₂ nanotubes, namely chemical template method, electrochemical method and hydrothermal method.

1.2.1. Chemical template method

The chemical template method involves assembling nanostructured primitive units into the porous template that forms nanotube structure. In the process of preparation of TiO₂ nanotube template, first, a porous alumina is prepared by anodizing, which is used as a template later, and then impregnates titanium-containing compound into the template by sol-gel method. After turning titanium-containing compound that entered into the porous alumina template into the metal oxide that possesses a template with a similar pore diameter and morphology of nanotube structure by a high temperature annealing process, porous alumina template is then dissolved with concentrated alkali. Since the metal oxide is not dissolved in concentrated alkali, metal oxide nanotubes such as TiO₂ nanotubes can be obtained, which have similar pore morphology to porous alumina template after washing by water. Martin et al. [11–13] successfully prepared nanotubes of TiO₂, Co₃O₄, MnO₂, WO₃ and ZnO and other metal oxides using this method.

1.2.2. Electrochemical method (anodic oxidation method)

Anodic oxidation method uses metal as an anode. Under the influence of applied electric field and electrolyte solution, electrochemical oxidation of the metal appears. Thereby a metal oxide film is produced on the surface of a metal. The formed metal oxide film will gradually dissolve because of the chemical reaction caused by the response plasma in electrolyte solution. The regional of chemical dissolution of metal oxide film is in nanoscale level. Therefore, when the speed of producing metal oxide by electric film dissolution is larger than the rate of chemical

dissolution, the oxide film is ever thickening and accompanied by numerous nanopore deepening constantly caused by chemical dissolution. When the speed of producing metal oxide by electric film dissolution is equal to the rate of chemical dissolution, the thickness of the oxide film and the depth of the nanopores do not change. At this time, a certain thickness oxide film with a metal oxide nanotube structure is ready. With the controlling of the different experimental conditions in certain electrolyte, we can prepare TNTA with different diameters and lengths by anodizing. In 2001, Grimes [14] first reported that the TNTA with ordered arrangement can be obtained at room temperature after directly anodizing for pure titanium sheet in an HF aqueous solution. Grimes [10] studied the growth of the nanotubes changes under different conditions of the anodizing electrolyte. The length of the nanotubes can be increased when the electrolyte exhibits weak acid. In the case of organic phase electrolyte, the tube walls are smoother and the tube length can also reach about a hundred micrometers.

1.2.3. Hydrothermal method

Since the hydrothermal preparation method is simple and cheap, it is widely used in industrial production processes. TiO₂ nanotubes prepared by this way are typically entwined and disorderly: first preparing TiO₂ nanoparticles, and then mixing the nanoparticles with strong alkaline solution. Under conditions of high temperature and pressure, monolayer nanosheets curl of TiO₂ in the alkali solution appears. Its formation mechanism is similar to that of multi-walled carbon nanotubes; it is a combination process from one-dimensional to two-dimensional and three-dimensional. After forming the TiO₂ nanotubes, the product is neutralized by weak acid to neutralize the strong alkaline solution, and centrifuging it to get powdery TiO₂ nanotubes. Using this method, Kasu's team processed the TiO₂ nanoparticles powder and NaOH solution at 110°C, then washed the reactants with water and hydrochloric acid and finally get TiO₂ nanotubes [15].

2. Intrinsic and surface-modified TiO₂ nanotubes gas sensors

2.1. Intrinsic TiO₂ nanotubes gas sensors

2.1.1. Investigation of gas-sensing simulation of intrinsic TiO₂ nanotubes

Three SF₆ decomposed gases, namely SO₂, SOF₂, and SO₂F₂, are chosen as probe gases because they are the main by-products in the decomposition of SF₆ under PD. The adsorption behaviors of these gases on an anatase (101) surface are studied using the first principles density functional theory (DFT) calculations.

2.1.1.1. Adsorption models and calculation methods

The optimal lattice size of bulk anatase given in MS is $3.776 \times 3.776 \times 9.486 \text{ \AA}^3$, which is very small compared with the size of a single TiO₂ nanotube. Thus, the gas molecules adsorbed in a small area of the TNTAs surface are simulated, and the nanotube-array structure is not taken into account. The prepared TNTAs are calcined at a high temperature in an oxygen-rich

environment, and oxygen atoms should occupy the oxygen vacancies on the TNTAs surface [16]. The phenomenon is consistent with the findings that many thermodynamically stable (101) facets dominate the surface of most anatase nanocrystals [17]. Therefore, the gas-array interaction can be properly simulated on the anatase (101) surface.

Periodic boundary model is adopted in this work, and the 2 × 2 supercell of the anatase (101) surface is created in MS, as shown in **Figure 2**. The size of the supercell is 10.88 × 7.55 × 17.84 Å³. In order to avoid the interaction between adjacent cells which is induced by the periodic boundary condition, the vacuum layer above surface is about 12 Å. The atoms on the bottom layer are fixed, and the structure of the supercell is optimized.

The generalized gradient approximation (GGA) exchange-correlation function parameterized by Perdew, Burke, and Ernzerhof [18] is employed for the electron-electron exchange and correlation interactions. Moreover, the double numerical basis set plus polarization functions (DNP) [19, 20] are used. All optimized structures are obtained with a precision of 1 × 10⁻⁵ Ha for energy, 2 × 10⁻³ Ha/Å for force, and 5 × 10⁻³ Å for displacement, the convergence threshold for the electronic self-consistent field is set to 1 × 10⁻⁶ Ha. A Fermi smearing of 5 × 10⁻⁴ Ha is used. To speed up the convergence and reduce calculation time, the DIIS (direct inversion in an iterative subspace) is used at the same time. The Brillouin zone is sampled at 2 × 3 × 1 *k*-mesh [21]. All spin-unrestricted DFT calculations are performed using the Dmol³ package [19, 20].

The band gap is 2.16 eV, which is closer to other simulation results [22, 23] but smaller than the experimental gap (3.24 eV [24]). The reason for this is the well-known deficiency of the GGA arithmetic [25] in which DFT maps the problem of *N* interacting electrons onto a system of *N* non-interacting fictitious particles. Therefore, the calculation scheme is effective, and the results and conclusions are reasonably reliable.

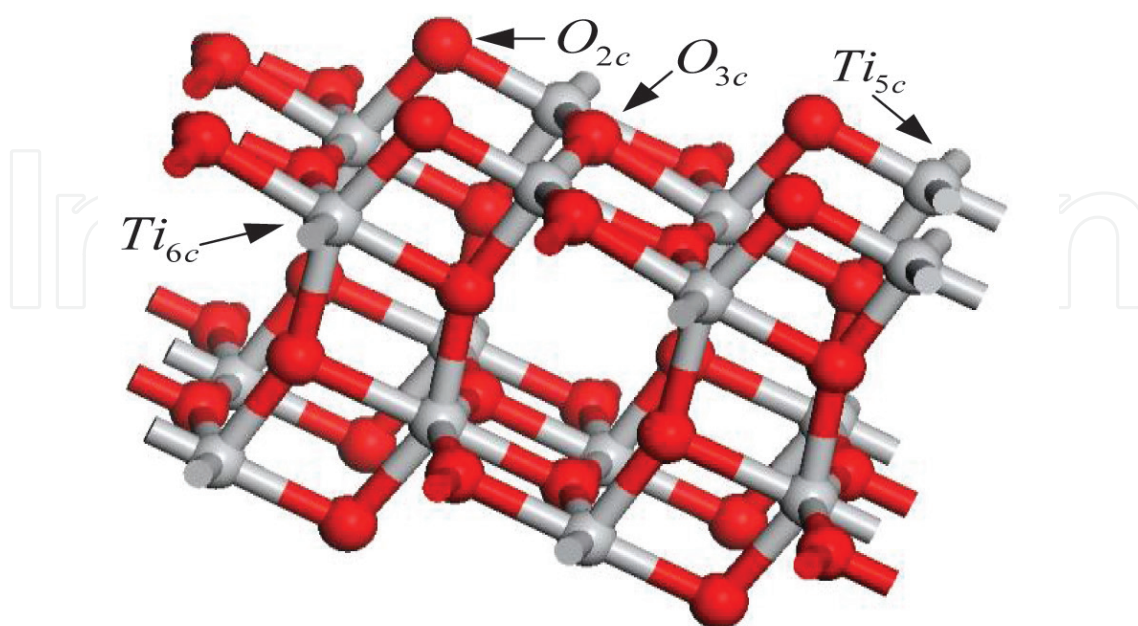


Figure 2. 2 × 2 supercell of the anatase (101) surface.

The active atoms of the anatase (101) surface are Ti_{5c} and O_{2c} as shown in **Figure 2**. **Figure 3** shows band structure of the optimized supercell. To find the most stable adsorption structures, the three gas molecules should approach the active atoms on the surface in different orientations and behaviors. **Figure 4** shows the most stable adsorption structures of the three gas molecules.

2.1.1.2. Adsorption parameters and analysis

The gas-surface interaction can be described using the adsorption energy E_{ad} defined as $E_{ad} = E_{surf/gas} - E_{gas} - E_{surf}$, where E_{gas} is the energy of one isolated gas molecule in its optimized structure, E_{surf} is the total energy of the TiO₂ structure, and $E_{surf/gas}$ is the total energy of the adsorption structure [1]. $E_{ad} < 0$ means that the adsorption process is exothermic and spontaneous.

The change in charge distribution should be known. Therefore, the charge transfer q is calculated using the Mulliken population analysis and is defined as the charge variation of isolated gas molecules when it is adsorbed [1]. A positive q value means that the charge is transferred from the molecule to the anatase surface. The binding distance d is defined as the nearest distance between the molecule and the surface. The calculated adsorption parameters are shown in **Table 1**.

The adsorption energies are negative, indicating that the adsorptions are exothermic and spontaneous. The values of energy released in the adsorptions are SO₂ > SOF₂ > SO₂F₂, and all are small (<0.6 eV). This finding indicates that the molecules of the three gases are physisorbed, not chemisorbed, on the anatase (101) surface. Thus, gas molecules cannot effectively be adsorbed

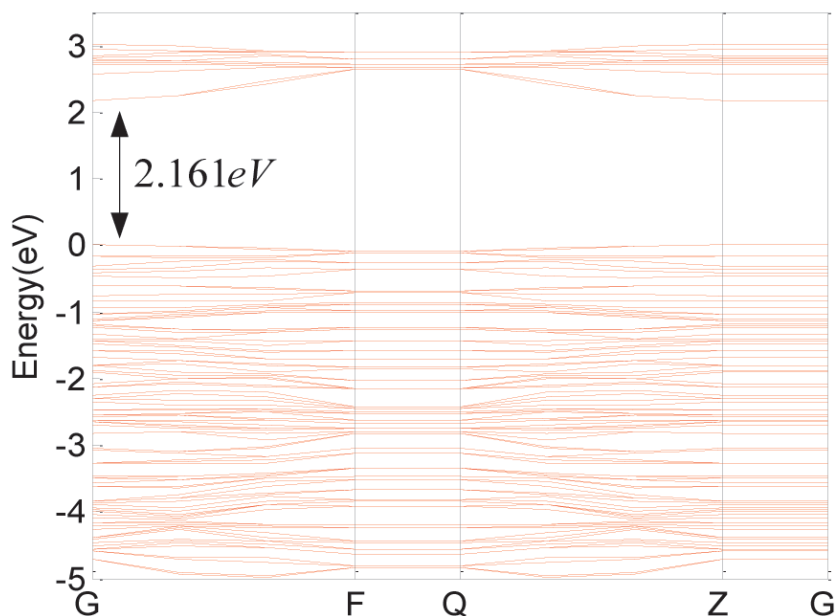


Figure 3. Band structure of the optimized supercell.

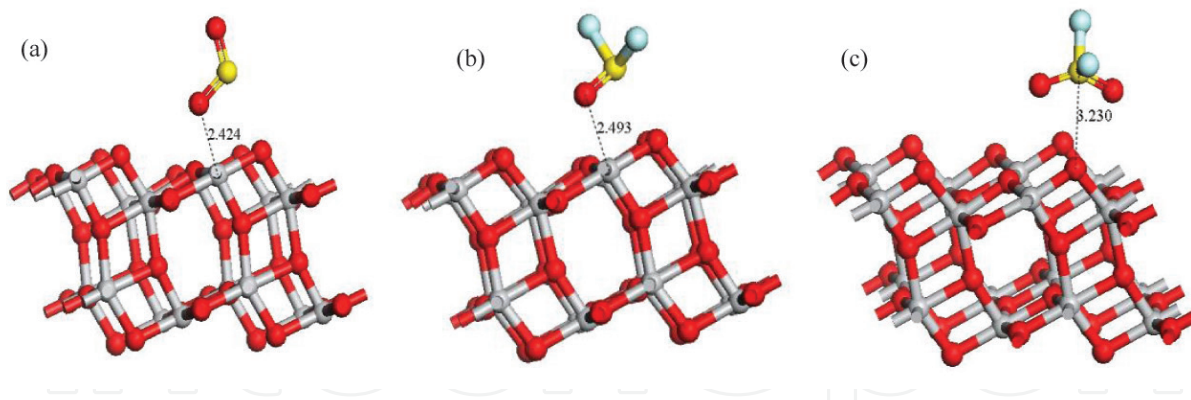


Figure 4. Optimized geometric structures of (a) SO₂, (b) SOF₂, and (c) SO₂F₂ adsorbed on the anatase (101) surface. Ti and O atoms are in gray and red, respectively. Binding distances are in Å.

System	Structure	E_{ad}/eV	q/e	$d/\text{Å}$
SO ₂	a	-0.343	0.094	2.424
SOF ₂	b	-0.275	0.043	2.493
SO ₂ F ₂	c	-0.186	0.008	3.230

Table 1. Calculated adsorption energy, charge transfer, and binding distance.

on TNTAs at room temperature because of the small adsorption energy, indicating that the experimental responses of the three gases may also be very small at room temperature. When the temperature is high, the Ti_{5c}-O_{2c} bonds will be stretched with the increased temperature, and the interactions between the molecules and surface become stronger. Under this condition, the molecules can be chemisorbed on the surface, which can explain the high responses in the sensing experiment. The adsorption energy of SO₂ is the largest of the three gases, which shows that the adsorption of SO₂ is the strongest; it is firmly absorbed and difficult to desorb.

The three gases all behave as charge donors. The charge transfer of SO₂ is more than twice than that of SOF₂, and for SO₂F₂, it is only 0.008 e. This finding indicates that SO₂ can provide more electrons to the surface and that the surface has a better sensitivity to SO₂.

The highest occupied molecular orbital (HOMO) energy level and lowest unoccupied molecular orbital (LUMO) energy level of the three gas molecules and of the anatase (101) surface are calculated according to molecular orbital theory. By analyzing the HOMO and LUMO, whether the gases easily interact with the anatase (101), surface can be estimated. E_1 and E_2 are defined as follows:

$$\begin{aligned} E_1 &= \left| E_{HOMO(TiO_2)} - E_{LUMO(gas)} \right| \\ E_2 &= \left| E_{LUMO(TiO_2)} - E_{HOMO(gas)} \right| \end{aligned} \quad (1)$$

If E_1 is small, the charge is more easily transferred to the gas molecules from the surface. If E_2 is small, the charge is more easily transferred to the surface from the gas molecules. The calculated E_{HOMO} , E_{LUMO} , E_1 , and E_2 are listed in **Table 2**.

System	E_{HOMO}/eV	E_{LUMO}/eV	E_1/eV	E_2/eV
TiO ₂	-7.257	-5.093	/	/
SO ₂	-8.000	-4.669	2.587	2.917
SOF ₂	-8.536	-3.072	4.185	3.453
SO ₂ F ₂	-9.145	-2.628	4.628	4.062

Table 2. Energy frontier molecular orbital and the energy difference.

Both the E_1 and E_2 of SO₂ are smaller than those of the other two gases. This finding shows that SO₂ easily interacts with the anatase (101) surface and that the charge transfer is also the easiest between them. SO₂F₂ interacting with the surface is relatively difficult. Here, we also find that the anatase (101) surface is more sensitive to SO₂ than to SOF₂, and the sensitivity of the surface to SOF₂ is better than that to SO₂F₂.

The energy gap of the adsorption structure can be calculated through the energy levels of the HOMO and LUMO defined as E_g :

$$E_g = |E_{HOMO} - E_{LUMO}| \quad (2)$$

The energy gap width determines how much energy an electron needs to jump into the LUMO from the HOMO. The wider the gap, the more energy is required and the more difficult it is for electrons to transfer between the valence band (VB) and the conduction band (CB). **Table 3** shows the energy gaps. The adsorption of SO₂ on the anatase (101) surface reduces the energy gap width and improves the electron transfer of the surface. However, the adsorption of SOF₂ and SO₂F₂ cannot do so. Therefore, TNTAs are much more responsive to SO₂ gas than to SOF₂ and SO₂F₂.

The molecular structures of the gases are also analyzed based on valence bond theory (VBT) combined with molecular orbital theory. A three-center four-electron pi bond exists in the SO₂ molecule, and the pi bond contains five orbitals that are hybridized by a 3p orbital, two 3d orbitals in the S atom, and a 3p orbital in each O atom. This finding indicates that the pi bond consists of some 3d orbitals. Four electrons occupy the two lower orbitals (i.e., HOMO and HOMO-1) of the pi bond, and the middle orbital of the pi bond is unoccupied (LUMO). However, the d-p pi bond exists between the S atom and the O atom in the SOF₂ and SO₂F₂ molecules. The S atom in SOF₂ has one lone pair of electrons, but not the SO₂F₂. Therefore, the

System	E_{HOMO}/eV	E_{LUMO}/eV	E_g/eV
TiO ₂	-7.257	-5.093	2.164
TiO ₂ -SO ₂	-7.134	-5.607	1.527
TiO ₂ -SOF ₂	-7.208	-5.053	2.155
TiO ₂ -SO ₂ F ₂	-7.204	-5.047	2.156

Table 3. Energy gaps of the adsorption structures and structures without adsorption.

SO₂F₂ molecule is more stable than the SOF₂ molecule. Moreover, the activities of the gas molecules can be compared by obtaining the difference between E_{HOMO} and E_{LUMO} . **Table 4** shows ΔE , which is defined as $\Delta E = E_{\text{LUMO (gas)}} - E_{\text{HOMO (gas)}}$. Based on the VBT analysis and the data in **Table 4**, the pi bond in SO₂ is more active than the d-p pi bond in SOF₂ and SO₂F₂. Moreover, SO₂ is easy to interact with the anatase (101) surface.

To investigate the influence of adsorbed gas molecules on the electronic property of the anatase (101) surface, the total density of states (TDOS) of the adsorption system and the projected density of states (PDOS) of adsorbed gas molecules calculated using MS are given in **Figure 5**. The Fermi level is aligned at zero. As shown in **Figure 5**, when the molecules of the three gases are adsorbed on the surface, the Fermi levels of those still on top of the VB change little. This finding indicates the formation of a depletion region on the surface, and only a few charge carriers are present in this region. Therefore, the surface presents high resistivity.

The TODSs of the SOF₂ and SO₂F₂ adsorption systems remain nearly unchanged compared with the system without adsorption, which indicates that the adsorbed SOF₂ and SO₂F₂ induce little change to the electronic property of the (101) surface. An unapparent density peak of around 2.8 eV exists in the PDOS of SOF₂. On the other hand, the adsorbed SO₂ induces noticeable change to the electronic property of the (101) surface. The SO₂ adsorption introduces an impurity state near the CB, as shown in **Figure 6**, resulting in a narrowing of the band gap (which changes from 2.161 to 1.527 eV). The unoccupied impurity state is a surface state of the anatase (101) surface, which can capture or release electrons or form a composite center, improving the conductive performance of the surface. The PDOSs of p orbitals that contribute to the impurity state and the orbitals that contain the 3p orbital of the S atom and the 2p orbital of the O atom (near the surface in **Figure 4**) are shown in **Figure 7**.

2.1.2. Preparation and surface characterization of intrinsic TiO₂ nanotubes

The present study generated a TNTA by an anodic oxidation method using a two-electrode system [1]. A platinum metal piece was used as cathode, whereas a titanium piece was used as anode. The experimental processes are as follows: first, 0.5-mm-thick Ti foil (area of 0.8 cm × 2.0 cm and purity of 99.94%) was burnished with sandpaper, soaked in 30% HCl solution, and heated to 80°C for 20 min to remove the surface oxidation layer [1]. Then, the Ti pieces were cleaned by washing with deionized water. The clean Ti pieces acted as the anode, whereas the platinum pieces acted as the cathode in the two-electrode electrochemical electrolysis pool. Between the two electrodes, a constant 20 V of anodic oxidation was applied continuously for 2 h. The electrolyte concentration was 0.1 M HF solution, and the electrolyte pH value was tested using a Model 3000 pH meter [1]. Magnetic stirring was applied to ensure the uniformity of the Ti electrode surface electric current and temperature in the oxidation process and

Gas	SO ₂	SOF ₂	SO ₂ F ₂
$\Delta E/\text{eV}$	3.330	5.464	6.517

Table 4. Difference between HOMO and LUMO.

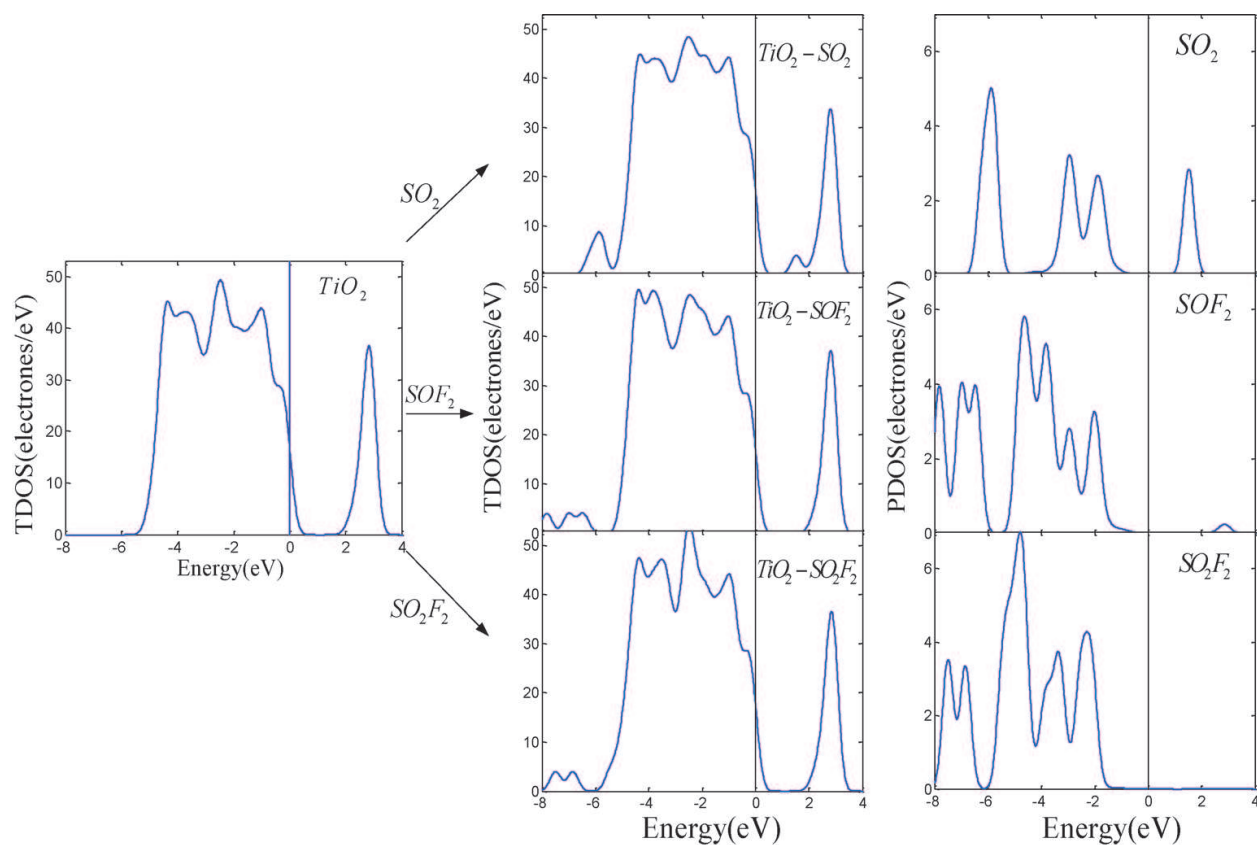


Figure 5. The TDOS of adsorption systems and the PDOS of adsorbed gas molecules.

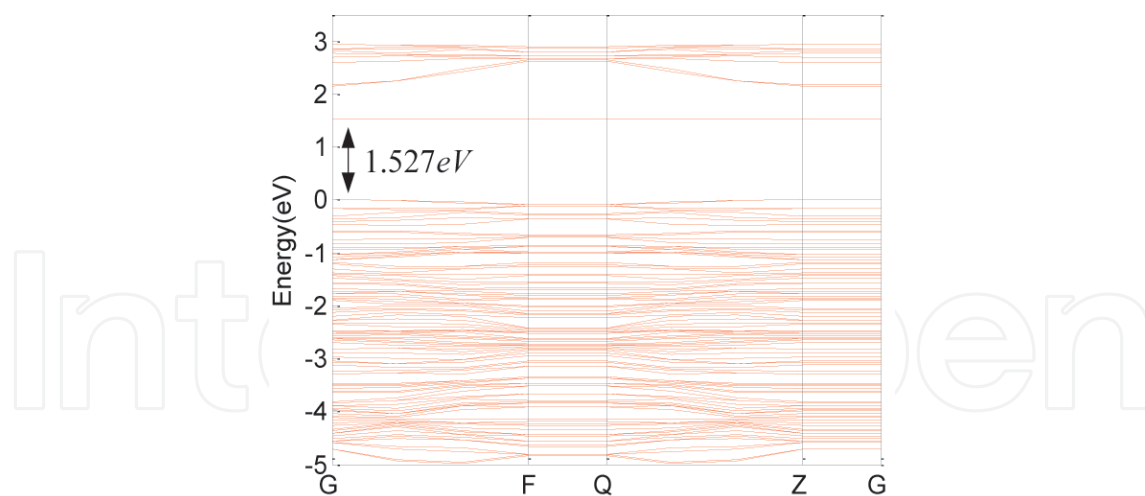


Figure 6. Band structure of the $\text{TiO}_2\text{-SO}_2$ adsorption system.

reduce the influence of the double electric layer between the electrolyte and electrode interface [1]. After the reaction, the TNTA was cleaned by washing with deionized water, dried in air heated from $2^\circ\text{C}/\text{min}$ to 500°C in a muffle furnace for 1 h, and then removed after the temperature dropped to room temperature [1].

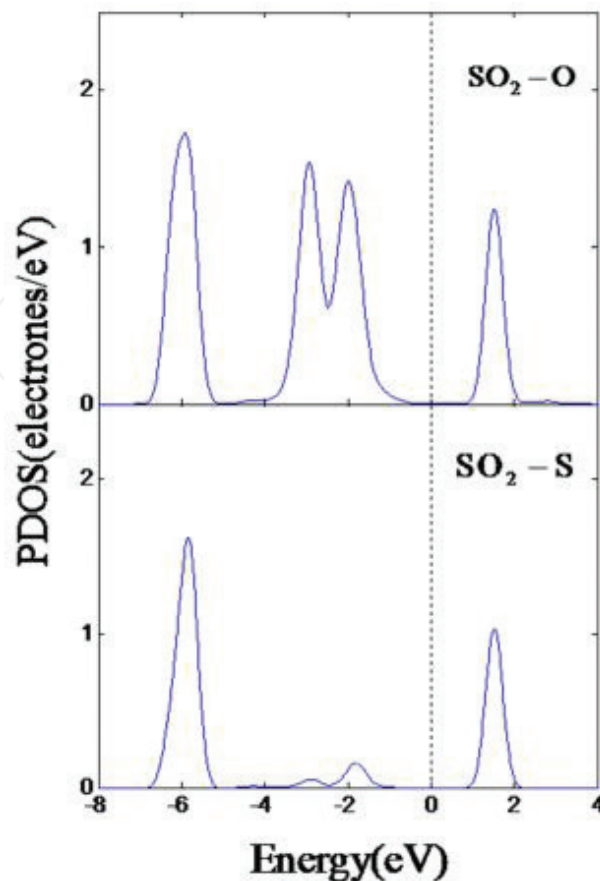


Figure 7. PDOS of the p orbitals of impurity state.

Figure 8 shows the scanning electron microscopy (SEM) images of the TNTAs. As observed from the SEM images, the TNTAs are highly ordered and directionally grown, the pipe diameter of which is about 80 nm, length is about 300 nm, and thickness is about 10 nm. The main effect of having an ordered structure is to further improve the area's effective adsorption area. The schematic diagram of TNTAs is shown in Figure 9.

Figure 10 shows the X-ray diffraction spectrum diagram of the TNTAs. The strong (101) facet peak of anatase (A in the figure) exists at $2\theta = 25.3^\circ$, and the weak strong (110) facet peak of rutile exists at $2\theta = 27.4^\circ$ (R in the figure). These findings indicate that TNTAs are mainly anatase, and a small amount of the rutile phase is observed.

2.1.2.1. Gas-sensing experiments of intrinsic TiO₂ nanotubes sensors

Figure 11 presents the detection test device for the TNTA sensor response measurement of the SF₆ decomposition products [1]. Shown in the figure are the following: (1) quartz glass tube; (2) thermal resistance probe; (3) carbon nanotube sensors; (4) ceramic heating slices; (5) vacuum form; (6) vacuum pump; (7) vent ducts; (8) terminals; (9) AC regulator; (10) temperature display apparatus; (11) impedance analyzer; (12) gas flow meter; and (13) inlet ducts [1].

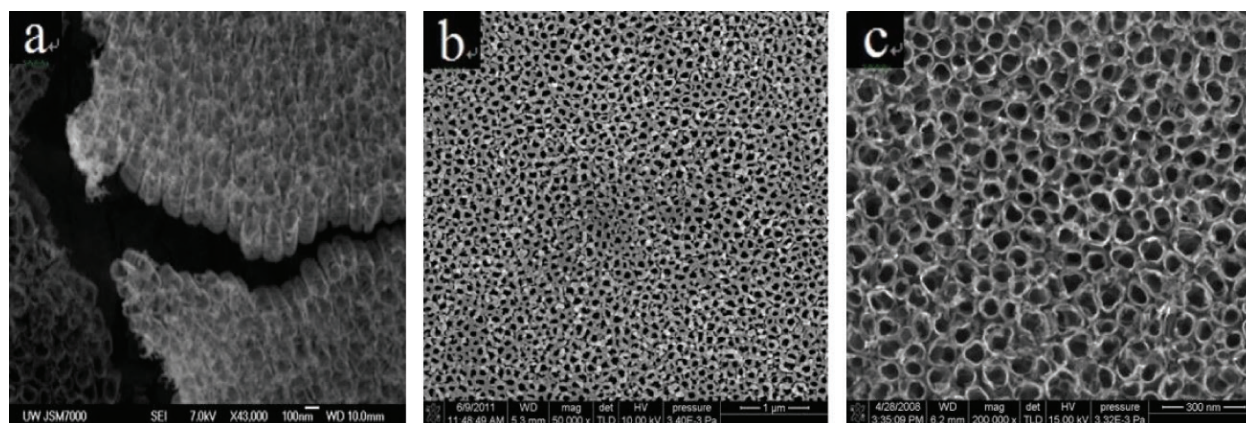


Figure 8. SEM images of TNTAs: (a) side view, (b) front view, (c) front amplification view.

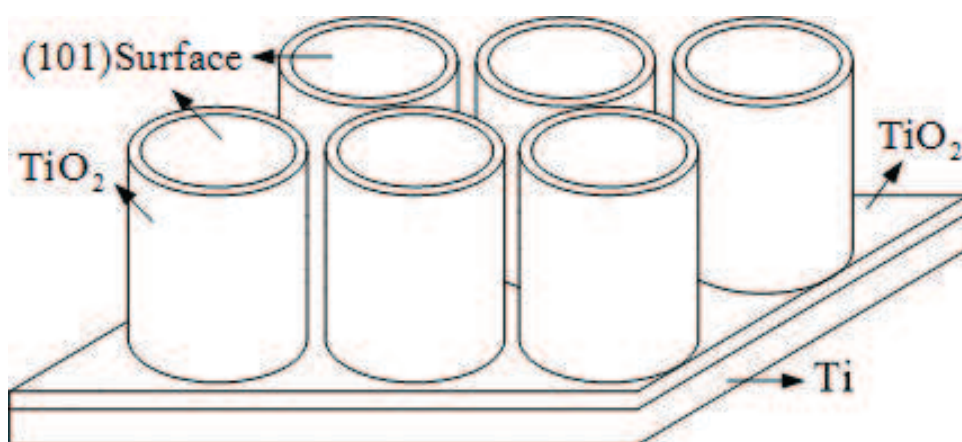


Figure 9. Schematic diagram of TNTAs.

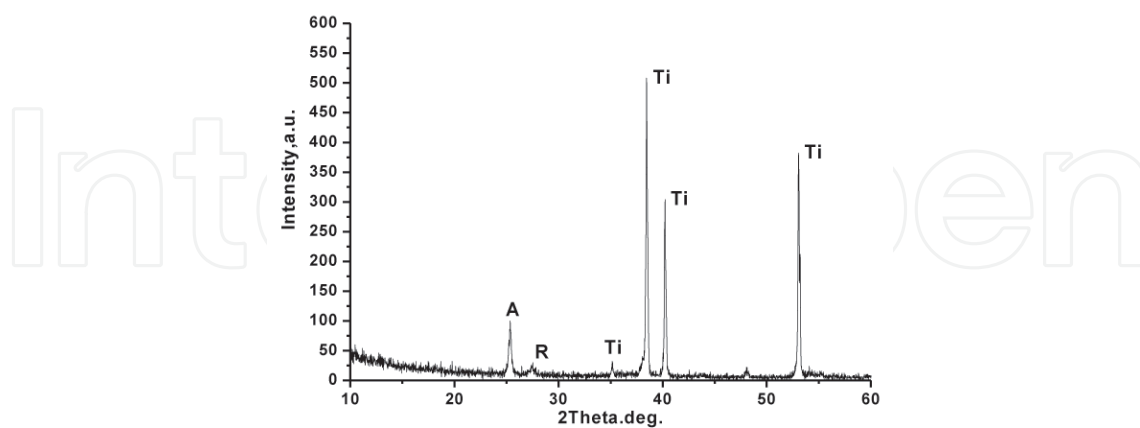


Figure 10. X-ray diffraction pattern of TNTAs.

The tested gases are SO₂, SOF₂, and SO₂F₂, which have a concentration of 50 μL/L, and N₂ is used as the carrier gas [26]. The response $R\%$ is defined as the relative variation of the sensor's resistance: $(R_g - R_0)/R_0$, where R_g is the resistance of the sensor to the relevant gas, and R_0 is pure

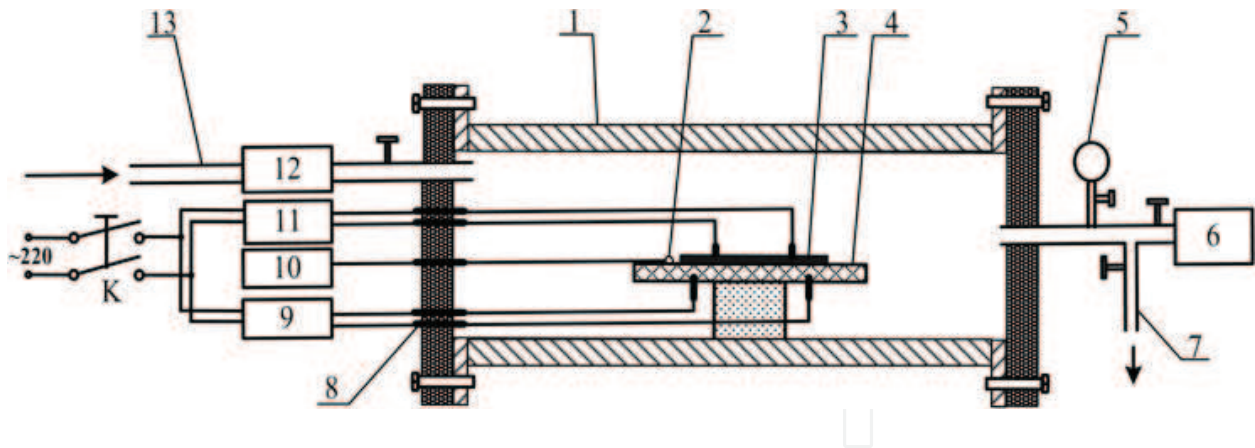


Figure 11. Detection test device for the TNTA sensor response measurement of SF₆ decomposition products.

N₂ [26]. The factors that influenced the response are analyzed comparatively, and the sensing mechanism of the temperature characteristic curves is explained based on the simulation results.

The responses of TNTAs to the 50 μL/L gases are shown in Figure 12. At 20°C, the response of SO₂ is slightly higher than that of SOF₂ and SO₂F₂, and the responses of SOF₂ and SO₂F₂ are both small. When the temperature is above 120°C, the response of SO₂ is much higher than that of the two gases. The response of SOF₂ is slightly higher than that of SO₂F₂. This phenomenon matches the simulated findings. Therefore, the study concludes that the response R% depends on the impurity state introduced by the adsorbed gas molecule, and the band structure influences by the impurity state.

The sensing mechanism of temperature characteristic curves is analyzed first.

When the temperature is low, the adsorbed gas molecules can provide a number of electrons to the semiconductor surface or reduce the band gap of the semiconductor; the thermal excita-

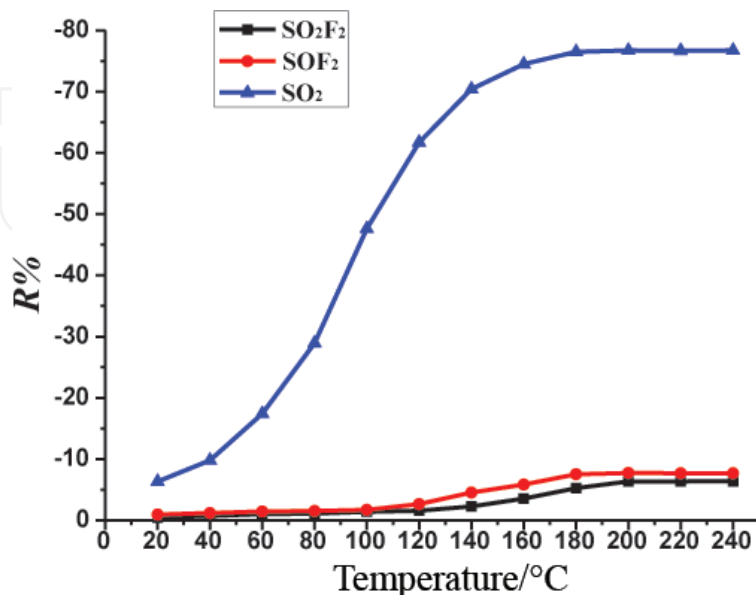


Figure 12. Temperature characteristic curves of the responses of 50 μL/L gases.

tion of the semiconductor remains weak. The electron depletion region of the surface remains, and the electron concentration variation is small. All sensing responses are low when the temperature is low. Conversely, when the temperature increases, thermal excitation begins to play a main role, and more electrons in the valence band exit to the conduction band, producing more hole electron pairs and greatly increasing the electron concentration. The adsorption of the three gases then provides electrons onto the semiconductor surface, introduces the impurity states, and reduces the band gap. Thus, more excited electrons enter into the CB from the VB, and their sensing response becomes higher.

The reason for the changes in the temperature characteristic response of SO₂, as shown in the curve in **Figure 12**, is discussed. The gas response at a high temperature is positively related to the concentration of thermally excited electrons and the adsorption amount of gas molecules. The adsorption amount increases when the temperature increases. However, if the temperature is too high, the thermal motions of the gas molecules become aggressive and a number of adsorbed gas molecules break away from the surface, decreasing the adsorption amount. The electrons produced by thermal excitation grow exponentially with the increasing temperature. Thus, the temperature characteristic response increases with the increasing temperature at first and then remains nearly unchanged.

The responses of SO₂ and SOF₂ are then compared. When the temperature is about 200°C, the response of SOF₂ is much lower than that of SO₂, and it is not sensitive to the varying temperature. The impurity state introduced by SO₂ has a great impact on the band structure and the SO₂ has a higher response because the impurity state introduced by SOF₂ has little effect on the band structure. The thermal excitation is weak, and only a few electrons are exit to the CB through the impurity states under 20°C. Therefore, the impurity states of SO₂ and SOF₂ have little effect on the band structure. However, TSO₂ provides more electrons to the surface, and the response of SO₂ is slightly high.

Finally, the responses of SOF₂ and SO₂F₂ are compared. SOF₂ provides more electrons to the surface than SO₂F₂, but the responses of the two gases are both small because the impurity states induced by the two adsorbed gases have little influence on the band structure. The electron depletion region on the surface also influences the low responses. Considering the comparative analysis of SO₂ and SOF₂, it can be concluded that, if the impurity state introduced by adsorbed gas has a greater impact on the band structure, the electrons provided by adsorbed gas will have a relatively large influence on the response at low temperatures.

When the temperature is high, the response of SOF₂ is slightly higher than that of SO₂F₂. The unapparent density peak around 2.8 eV in the PDOS of SOF₂ has a certain effect on the band structure, and some electrons in the VB exit to the CB, which promotes the response.

The difference between the responses to 50 μL/L SOF₂ and SO₂F₂ is not obvious in **Figure 12**; thus, we discuss the concentration response curves of SOF₂ and SO₂F₂ at 200°C in **Figure 13**. In **Figure 13**, with increased concentration, the increase in SO₂F₂ response is relatively larger than that of the SOF₂ response because the impurity state introduced by the increase in SOF₂ has a greater impact on the band structure.

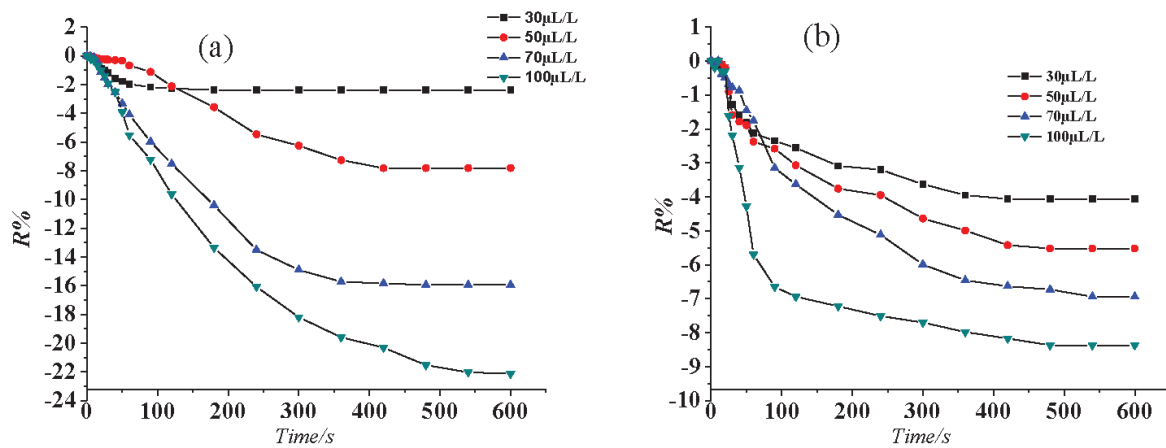


Figure 13. Response curves of SOF₂ (a) and SO₂F₂ (b) when the concentration varies at 200°C.

2.2. Pt-doped TiO₂ nanotubes sensors

The adsorptions of SO₂, SOF₂, and SO₂F₂ on Pt-modified anatase (101) surface are calculated, the effect of modified Pt on the adsorption behavior of gas molecules is analyzed, and the sensing mechanism of Pt-modified TNTA is also explained clearly [27]. In this study, we improve the sensing mechanism of Pt-modified TNTA and provide a theoretical basis for the detection of SF₆ decomposition components using the TNTA gas sensor [1, 28].

2.2.1. Investigation of gas-sensing simulation of Pt-doped TiO₂ nanotubes

2.2.1.1. Adsorption models and calculation methods

Figure 14 shows the adsorption structures of SO₂, SOF₂, and SO₂F₂ on the perfect (101) surface of Pt-modified anatase [1]. The adsorption parameters are shown in Table 5. Comparing the parameters in Table 5 [1] with the parameters in references [29, 30], we observed that the modified

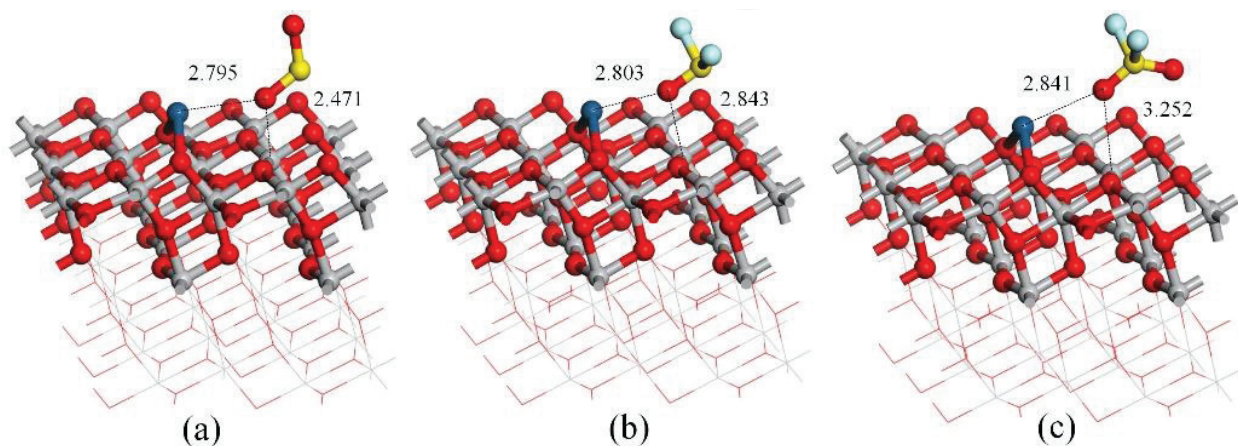


Figure 14. Adsorption structures of SO₂, SOF₂, and SO₂F₂ on the perfect (101) surface of Pt-modified anatase.

Adsorption site	Structure	Adsorption energy	Charge transfer	Bond distance
Perfect surface of the Pt-modified anatase surface	SO ₂ -TiO ₂ (a)	-0.3606	0.0920	2.471
	SOF ₂ -TiO ₂ (b)	-0.2811	0.0470	2.803
	SO ₂ F ₂ -TiO ₂ (c)	-0.0692	0.0110	2.841

Table 5. Adsorption parameters of the three gases adsorbed on the perfect (101) surface of Pt-modified anatase.

Pt atom has a slight influence on the adsorptions of the three gases on the perfect surface near the Pt atom [1]. The energy values of the three gases adsorbed on the anatase perfect surface are all still <0.6 eV. The charges in the adsorptions are still transferred from the molecules to the surface, which reveals that the three adsorptions are physisorptions [1]. This finding indicates that the adsorption performance of the perfect (101) surface of the Pt-modified anatase to the three gases is nearly unchanged [1]. **Figure 15** shows the DOS of the three adsorption structures [1]. We observed that the DOS is also nearly unchanged, and the state density near the Fermi level is mainly determined by the modified Pt atom. However, when the three gas molecules adsorb on the perfect (101) surface of the Pt-modified anatase, the conductivity of the surface is improved [1, 29].

2.2.1.2. Adsorption parameters and analysis

Figure 16 shows the adsorption structures of SO₂, SOF₂, and SO₂F₂ on the modified Pt atom [1]. The adsorption parameters are shown in **Table 6** [1]. When SO₂ is adsorbed, two situations, which depend on the initial structure, occur. One is the physisorption structure shown

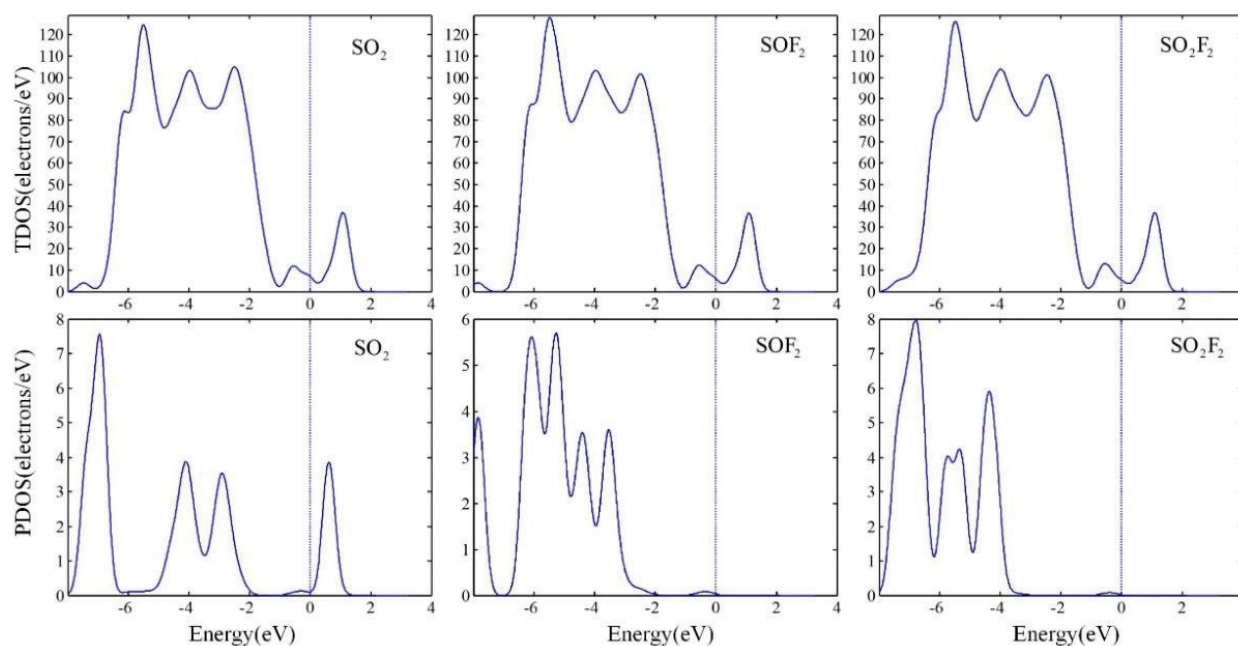


Figure 15. TDOSs of the adsorption structures of SO₂, SOF₂, and SO₂F₂ on the perfect (101) surface of Pt-modified anatase and PDOSs of the three gases in these structures.

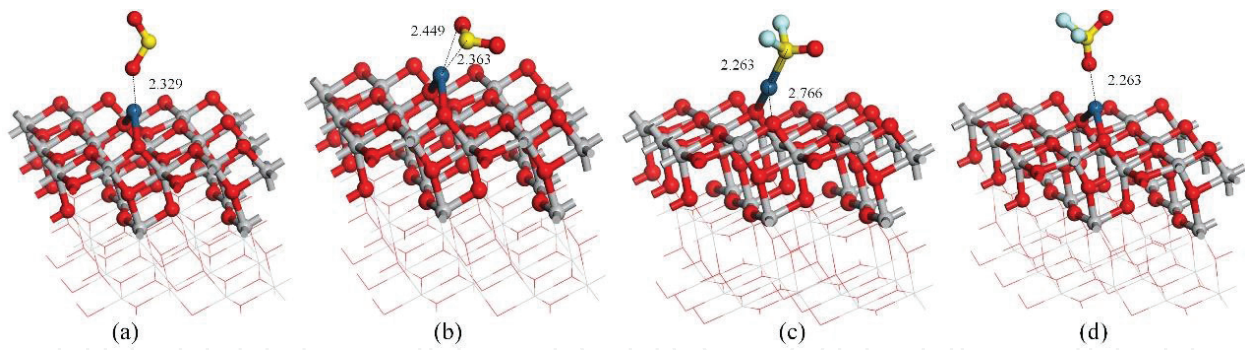


Figure 16. Adsorption structures of SO₂, SOF₂ and SO₂F₂ on the modified Pt atom of Pt-modified anatase.

in **Figure 16a** whose adsorption energy is -0.2394 eV. The other is the chemisorption structure shown in **Figure 16b** whose adsorption energy is -1.1009 eV. When SOF₂ is adsorbed, the physisorption and chemisorption situations occur. The chemisorption structure is shown in **Figure 16c**. The Pt atom has a stronger adsorption to the S atom in SOF₂ than the O or F atom [1]. Thus, the SOF₂ molecule is more easily chemisorbed on the Pt atom with the S atom, rather than physisorbed with the O or F atom [1].

When SO₂F₂ is adsorbed, the adsorptions are mainly physisorptions, such as the structure shown in **Figure 16d**. In addition, in a few initial structures, one S–F bond of SO₂F₂ may break and SO₂F₂ would be chemisorbed on the Pt atom. **Figure 17** shows the DOS of the three gases adsorbed on the Pt atom [1]. The adsorbed gas molecules contributed to the state density near the Fermi level, which changes the electronic distribution of the area around the modified Pt atom and influences the conductivity of this area [1].

Considering that the actual size of the modified Pt nanoparticle is larger than a single gas atom, and the conductivity of the nanoparticle is good and stable, we assume that the adsorptions of the gas molecules on the surface of the nanoparticle have a slight influence on the conductivity of the nanoparticle [1]. The main effect of the nanoparticle is the catalytic decomposition of some gas molecules [1]. We also calculated the adsorptions of SO₂, SOF₂, and SO₂F₂ on the Pt (200) surface to verify this finding. The adsorption structures are shown in **Figure 18** [1]. In **Figure 18a** and **b** [1], we observed that SO₂ and SOF₂ form stable adsorption structures on the Pt (200) surface with the S atoms, which are similar to the structures on the single Pt atom of the anatase (101) surface. **Figure 18c** [1] is the stable adsorption structure of SO₂F₂ on the Pt (200) surface, which is different from the structure shown in **Figure 17d** [1], in that one

Adsorption site	Structure	Adsorption energy	Charge transfer	Bond distance
Adsorbed on the modified Pt atom	SO ₂ -TiO ₂ (a)	-0.2394	-0.115	2.329
	SO ₂ -TiO ₂ (b)	-1.1009	-0.292	2.363
	SOF ₂ -TiO ₂ (c)	-0.9416	-0.075	2.263
	SO ₂ F ₂ -TiO ₂ (d)	-0.0630	0.020	2.425

Table 6. Adsorption parameters of the three gases adsorbed on the modified Pt atom of Pt-modified anatase.

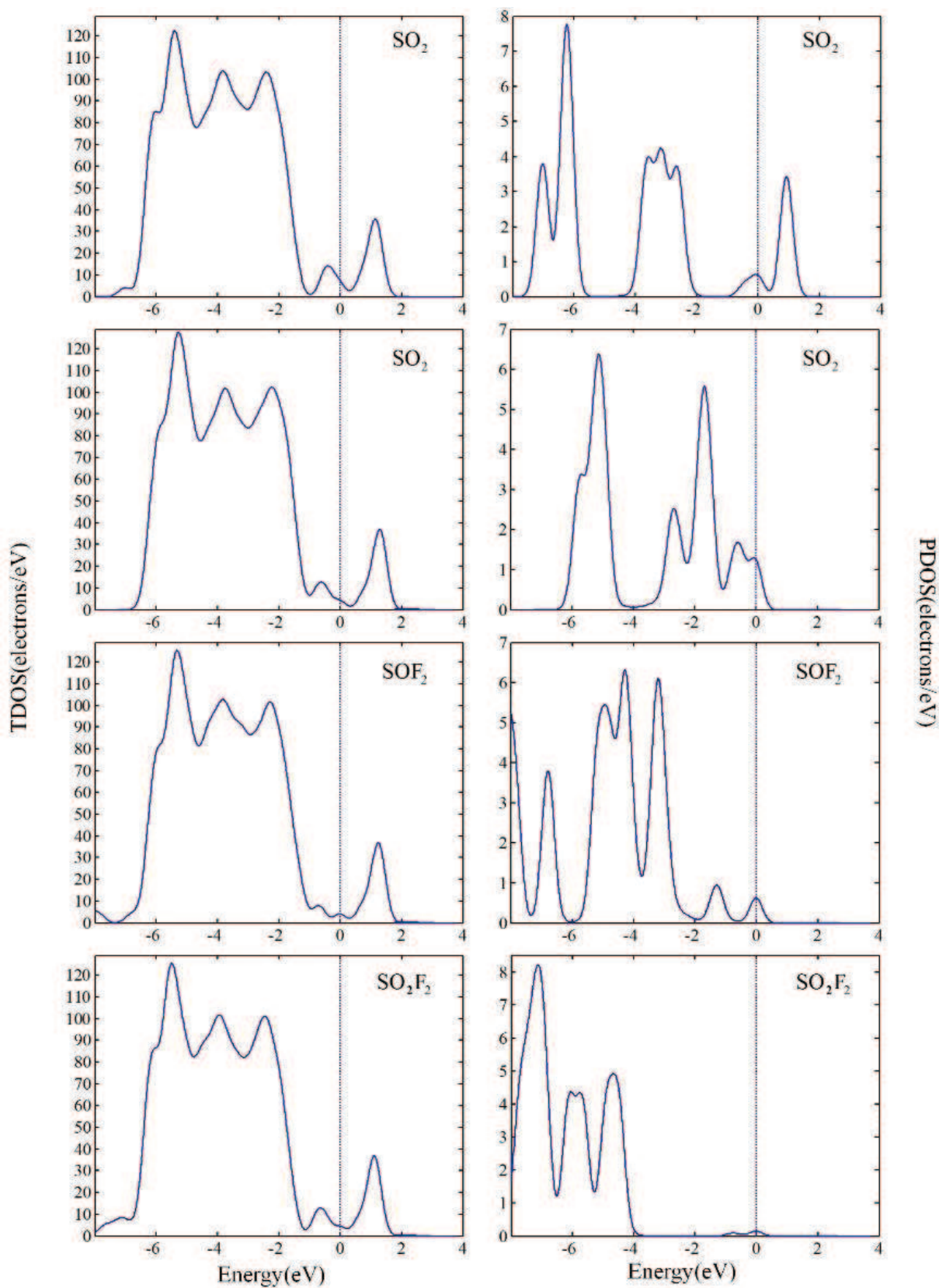


Figure 17. TDOSs of the adsorption structures of SO_2 , SOF_2 , and SO_2F_2 on the modified Pt atom of Pt-modified anatase and PDOSs of the three gases in these structures.

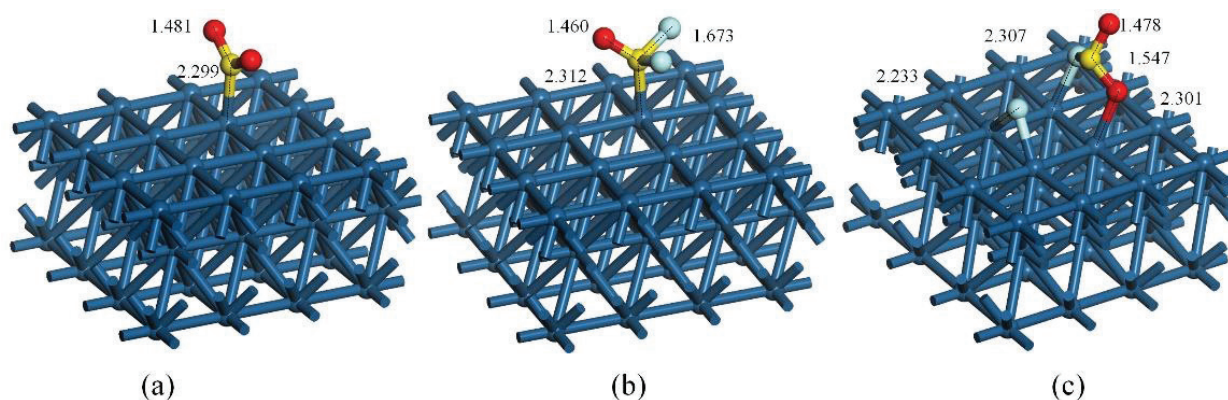


Figure 18. Adsorption structures of SO₂, SOF₂, and SO₂F₂ on the Pt (200) surface.

S–F bond of SO₂F₂ breaks, as shown in **Figure 18c** [1], and SO₂F₂ is chemisorbed on the Pt (200) surface. The Pt (200) surface supplies more electrons than a single Pt atom of the anatase (101) surface and the S–F bond more easily breaks. Thus, we conclude that, when adsorbed on the Pt nanoparticles of the TNTA surface, the SO₂F₂ gas molecules are more easily catalytically decomposed by the Pt nanoparticles than the SOF₂ molecules.

Figure 19 [1] shows the adsorption structures of SO₂, SOF₂, and SO₂F₂ on Pt and anatase. The adsorption parameters are shown in **Table 7**. From **Table 7** [1], we observed that the values of the adsorption energies of the three gases adsorbed on this site are relatively large, which indicates chemisorption [1]. The adsorption energy of SO₂F₂ is the largest and that of SOF₂ is the smallest. When SO₂ is adsorbed, the S atom of the SO₂ molecule bonds with the Pt atom, and one O atom of the SO₂ molecule bonds with the titanium (Ti) atom, as shown in **Figure 19a** [1]. When SOF₂ is adsorbed, the S atom of the SO₂ molecule also bonds with the Pt atom and one O atom of the SO₂ molecule bonds with the Ti atom, as shown in **Figure 19b** [1]. When SO₂F₂ is adsorbed, one S–F bond of SO₂F₂ breaks down. The S and F atoms bond with the Pt atom, with one O atom of the SO₂F₂ molecule bonding with the Ti atom, as shown in **Figure 19c**.

Figure 20 [1] shows the DOS of the three gases adsorbed on Pt and anatase. We observed that the adsorbed gas molecules contributed to the state density near the Fermi level, which also changes the electronic distribution of the area around this adsorption site. Considering the actual effect of Pt nanoparticles, we assume that this adsorption site is more active and the adsorptions of gas molecules on this site effectively connects the Pt nanoparticle surface and the anatase (101) surface, which may improve the conductivity performance of this area [1].

2.2.2. Preparation and surface characterization of Pt-doped TiO₂ nanotubes

The Pt-doped TiO₂NTs based on intrinsic TiO₂NTs were prepared using constant current method to deposit the Pt nanoparticles onto the TiO₂NT surface. Intrinsic TiO₂NTs were prepared through anodic oxidation [31], and a conventional three-electrode system with constant potential method is used to dope Pt nanoparticles into TiO₂NTs. In the three-electrode system, the intrinsic TiO₂NTs serve as the working electrode with a geometric area of 4.0 cm². The

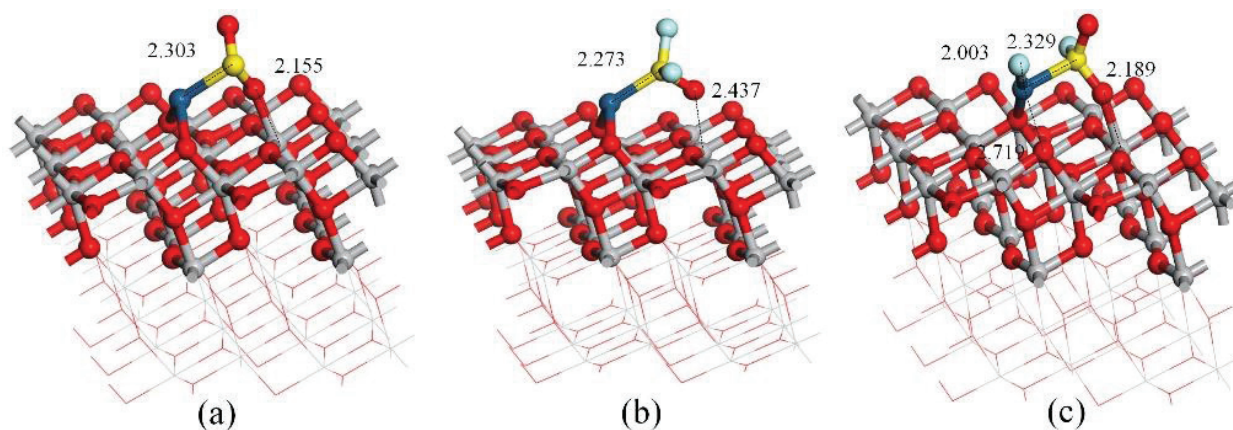


Figure 19. Adsorption structures of SO_2 , SOF_2 and SO_2F_2 on both Pt and anatase.

Adsorption site	Structure	Adsorption energy	Charge transfer	Bond distance
Adsorbed on Pt and anatase	$\text{SO}_2\text{-Pt-TiO}_2(\text{a})$	-1.4215	-0.2700	2.155
	$\text{SOF}_2\text{-Pt-TiO}_2(\text{b})$	-0.8405	-0.1930	2.273
	$\text{SO}_2\text{F}_2\text{-Pt-TiO}_2(\text{c})$	-1.6862	-0.7110	2.003

Table 7. Adsorption parameters of the three gases adsorbed on both of Pt and anatase.

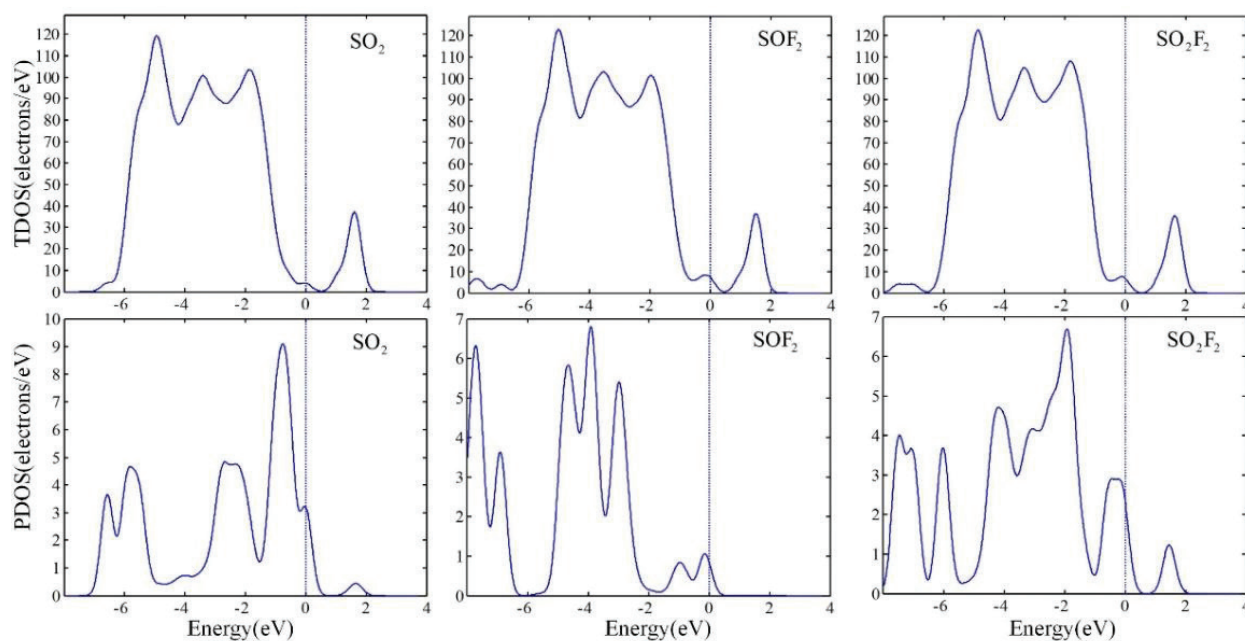


Figure 20. TDOSs of the adsorption structures of SO_2 , SOF_2 and SO_2F_2 on both of Pt and anatase and PDOSs of the three gases in these structures.

Ag/AgCl electrode is the reference electrode, and platinum electrode functions as the counter electrode. An electronic pulse signal was produced in the constant current control mode of the Shanghai Chen Hua CHI660D electrochemical analyzer. The electrolyte was an aqueous solution of H₂PtCl₆·6H₂O (1 g/L) and H₃BO₃ (20 g/L) at 50°C (pH = 4.4). After numerous exploratory experiments, the optimal parameters determined for the constant current method are as follows: current density of 0.1 mA/cm², and doping times of 10, 20, 30, and 40 s. In the deposition process, a magnetic stirrer is used to ensure that the liquid has a stable metal ion concentration.

Figure 21 shows the cyclic voltammetry curve of the four types of sensors with different amounts of doped Pt in 1.0 mol/L NaOH solution. Curves (a) to (d) correspond to the doping times of 10, 20, 30, and 40 s, respectively. During electrochemical deposition, Pt⁴⁺ in the electrolyte is reduced to Pt, as described in [32]; the sizes of the curve areas were compared to determine the amount of deposited Pt metal. The humps between -1.0 and 0.8 V in the four curves shown in **Figure 21** correspond to the hydrogen absorption and dehydrogenation processes of the Pt ions in NaOH solution [33]. The hump in curve (a) is not evident, and the humps in curves (b) to (d) are significant. Based on the size of each curve surrounding the area, we concluded that the amount of deposited Pt nanoparticles on the TiO₂NT surface is proportional to deposition time.

Figure 22 shows the SEM images of intrinsic and Pt-doped TiO₂NTs. **Figure 22a** shows the intrinsic TiO₂NTs, and **Figure 22b–e** presents the Pt-doped TiO₂NTs with deposition times of 10, 20, 30, and 40 s. The white objects around or above the tube wall in **Figure 22** are Pt nanoparticles. The SEM images show that the amount of Pt deposition increases with the deposition time. At 10 s, less Pt nanoparticles are deposited, and at 30 s, the Pt nanoparticles have moderate

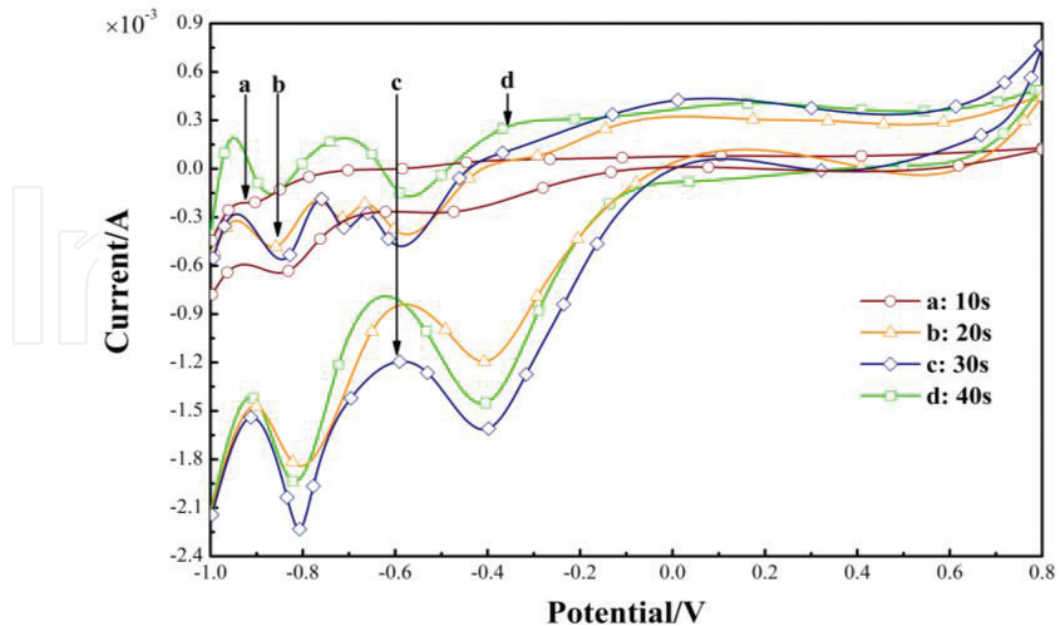


Figure 21. Cyclic voltammetry curve of sensors with different amounts of doped Pt in 1.0 mol/L NaOH.

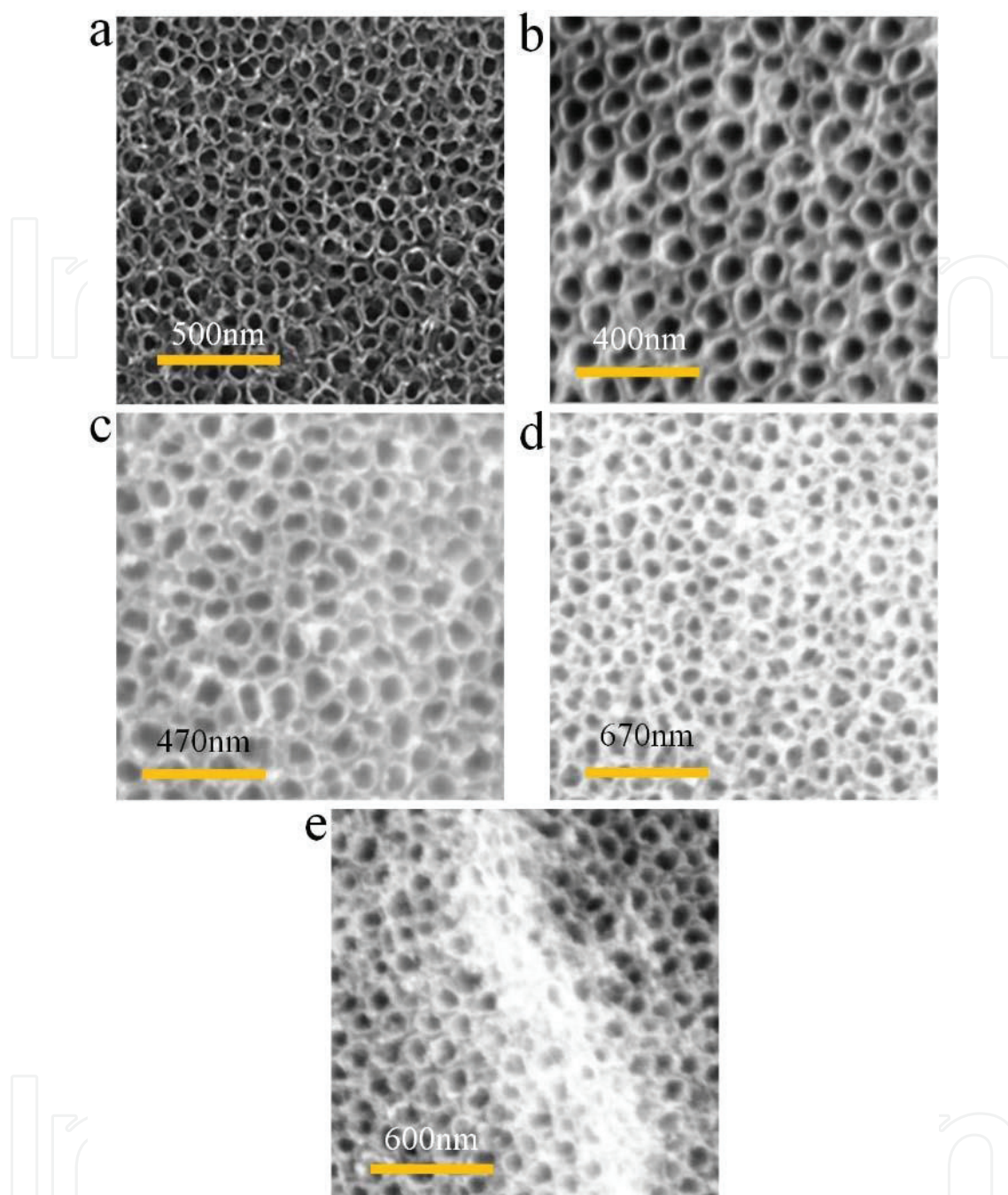


Figure 22. SEM images of intrinsic and Pt-doped TiO₂NTs.

sizes and are uniformly distributed. At 40 s, more Pt nanoparticles are deposited, and large tracts of these nanoparticles block the mouth of TiO₂NTs, as shown in **Figure 22e**.

Figure 23 shows that the intrinsic and Pt-doped TiO₂ NTs have strong anatase (101) crystal plane peak at $2\theta = 25.3^\circ$ (A in **Figure 23**). Pt (111) and (200) crystal surface peaks at $2\theta = 40.5^\circ$ and 46° were observed in the XRD patterns of the Pt-doped TiO₂ NTs.

However, no such peaks are found for the intrinsic TiO₂ NTs. This result shows that the constant potential method is useful when Pt nanoparticles are doped on TiO₂ NTs.

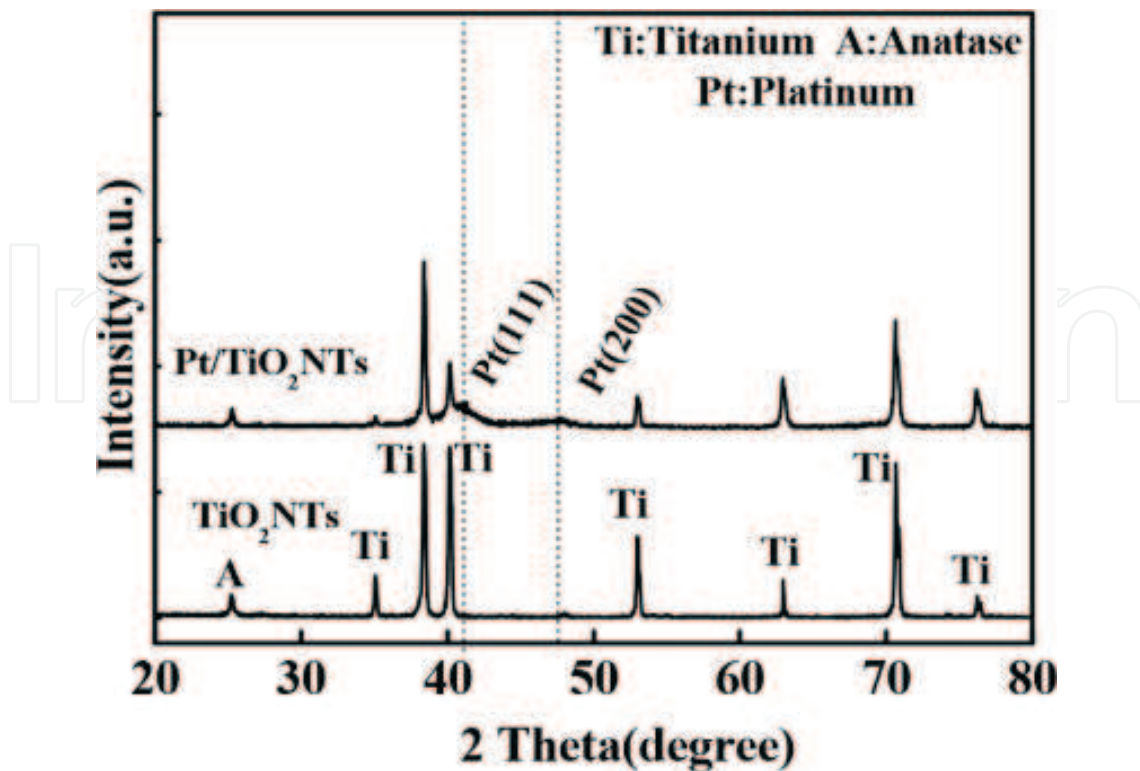


Figure 23. XRD patterns of Pt-doped TiO₂NTs.

2.2.3. Gas-sensing experiments of Pt-doped TiO₂ nanotubes sensors

The performance of gas-sensitive metal oxide material is significantly influenced by working temperature. Therefore, the gas-sensing responses of the sensors with different amounts of doped Pt were investigated under different operating temperatures for SOF₂, SO₂F₂, and SO₂ gases. The optimal operating temperatures of the sensors were also determined.

The prepared Pt-doped sensors were placed into the test device (Figure 11). The sensor surface was then controllably heated. In this experiment, the sensor gas-sensing characteristics of the sensors for SOF₂, SO₂F₂, and SO₂ gases at 100 ppm from 20 to 220°C were examined. The results are shown in Figure 24.

Figure 24 shows the resistance sensitivity curves of the sensors with different amounts of doped Pt for SOF₂, SO₂F₂, and SO₂. The figure shows that the gas response value of the sensor (i.e., resistance change rate, R%) increases with increasing sensor surface temperature. The optimal sensor operating temperature is approximately 160°C. When the temperature reaches 100–160°C, the largest response value is observed. As the temperature increases, the sensor response value begins to dramatically decrease. When the temperature reaches 200°C, the response value becomes small. The optimal operating temperatures and selectivity of the four sensors for the three decomposition component gases vary, as shown in Table 8.

The optimal operating temperature is 160, 150, 130, and 100°C at 10, 20, 30, and 40 s doping time, respectively. These results show that with increasing doping time, the optimal working

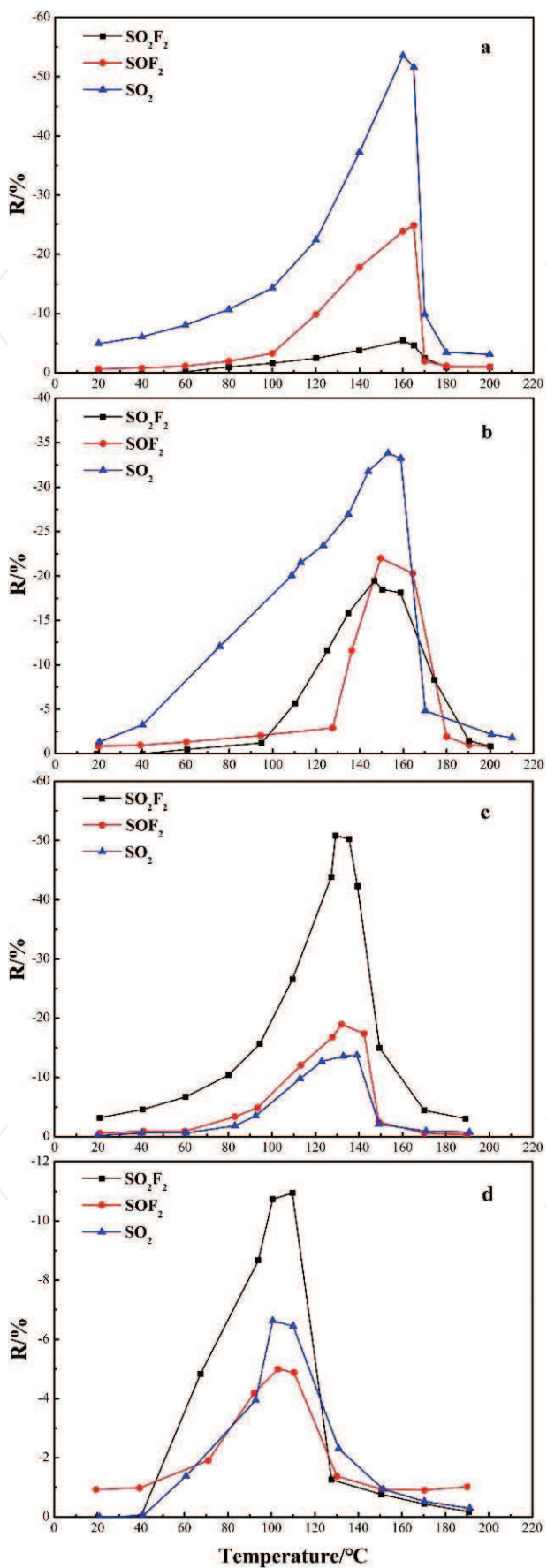


Figure 24. Sensitivity of sensors with different amounts of doped Pt with varying working temperatures.

Doping time	Optimal temperature	Sensitivity		
		SO ₂	SOF ₂	SO ₂ F ₂
10 s	160°C	-53.3%	-24.2%	-5.4%
20 s	150°C	-33.9%	-22.1%	-19.2%
30 s	130°C	-13.8%	-19.1%	-50.6%
40 s	100°C	-6.7%	-5.1%	-10.7%

Table 8. Sensitivity of Pt-doped sensors for 100 ppm SO₂, SOF₂ and SO₂F₂ at their optimum temperatures.

temperature of the sensor decreases. In addition, at the optimal temperature, the sensor with 10 s of doping time is the most sensitive to SO₂ at -53.3% but has the weakest response to SO₂F₂ at -5.4%. The sensor with 20 s of doping time is most sensitive to SO₂ at -33.9% but has weakest response to SO₂F₂ at -19.2%. The sensor with 30 s of doping time is most sensitive to SO₂F₂ at -50.6% but has weakest response to SO₂ at -13.7%. The SOF₂ gas response values of these three sensors remained almost unchanged. The sensor with 40 s of doping of time has significantly low responses for the three gases.

Compared with the intrinsic TiO₂NT sensor, the doped Pt nanoparticles alter the sensor surface microstructure and charge distribution. When the sensor surface temperature is higher than its optimum working temperature, the Pt nanoparticles improve the chemical desorption rate on the sensor surface. This result indicates that the desorption rate of a gas molecule is higher than its adsorption rate, and that the density of the gas molecule adsorbed onto the surface decreases, such that the response value of the sensor rapidly decreases. However, most parts of the tube mouth of the 40 s sensor are blocked by Pt nanoparticles; thus, the gas-sensing response value is highly reduced.

According to the experimental methods and procedures mentioned above, the four kinds of sensors function at their optimal operating temperatures. Their gas-sensing property curves are tested under SO₂, SOF₂, and SO₂F₂ gases at 25, 50, 75, and 100 ppm. The change rate of the sensor resistance (gas-sensing response value) was calculated at various concentrations. The linear relationship between the change rate of the sensor resistance and gas concentration was examined. Using the linear fit curve, we can also estimate the concentration of the gas using the sensor response value. After multiple experiments, the gas-sensing response values of the four sensors were found to increase with the experiment gas concentration, but for one kind of gas. Therefore, in the following section, only the 30 s sensor is considered, and its gas-sensing response curves were obtained at different gas concentrations. The experimental data of the remaining three sensors were obtained using the linear fit curve.

2.2.3.1. Gas-sensing properties of sensors with different amounts of doped Pt to SO₂ gas

Figure 25a shows that sensor with 30 s of doping time has resistance change rates of -2.0, -7.0, -10.0, and -13.8% for the SO₂ gas at 25, 50, 75, and 100 ppm, respectively. **Figure 25b** shows that sensor with 10 s doping time has response values of -10.7, -25.6, -36.0, and -53.2% for the four SO₂ concentrations. For the sensor with 20 s of doping time, the response values

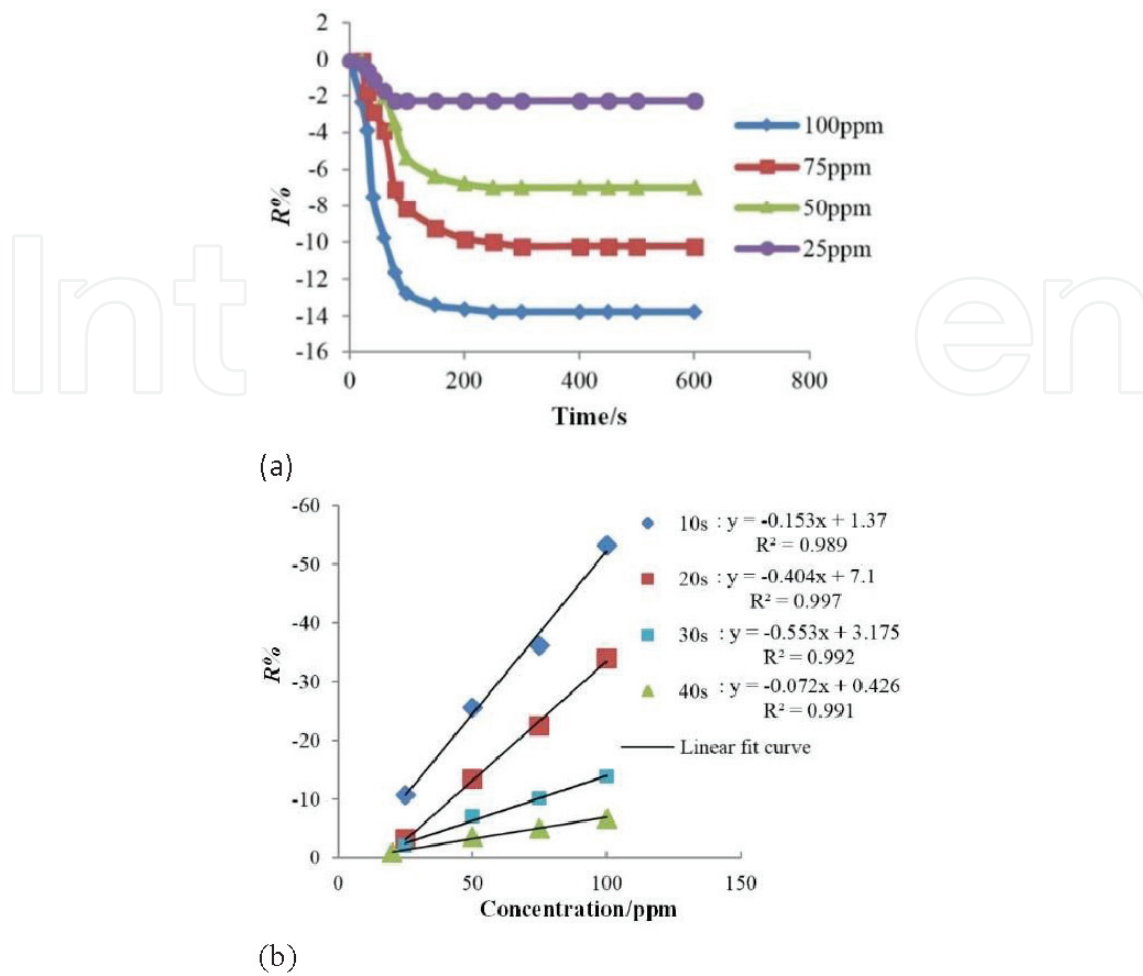


Figure 25. Response of four sensors with different amounts of doped Pt to varying concentrations of SO₂. (a) Gas-sensing response curves of 30 s sensor for different concentrations of SO₂ gas at 130°C. (b) Linear relationship between sensor response and gas concentration.

are -3.2, -13.4, -22.3, and -33.9% for the four SO₂ concentrations. Meanwhile, for the sensors with 40 s of doping time, response values are -0.8, -3.5, -5.0, and -6.7% for the four SO₂ concentrations. The sensitivities are shown in **Table 9**. The linear fit function and linear correlation coefficient are shown in **Figure 25b**.

Concentration	SO ₂			
	10 s	20 s	30 s	40 s
100 ppm	-53.2%	-33.9%	-13.8%	-6.7%
75 ppm	-36.0%	-22.3%	-10.0%	-5.0%
50 ppm	-25.6%	-13.4%	-7.0%	-3.5%
25 ppm	-10.7%	-3.2%	-2.0%	-0.8%

Table 9. Sensitivity of Pt-doped 30 s sensor to different concentrations of SO₂ at optimal working temperature.

2.2.3.2. Gas-sensing properties of sensors with different amounts of doped Pt for SO₂F₂ gas

Figure 26a shows the gas-sensing response curve of the sensor with 30 s doping time for SO₂F₂ at 25, 50, 75, and 100 ppm and 130°C. The resistance change rate is -3.5, -16.1, -32.1, and -50.6% for the different tested SO₂F₂ concentrations. **Figure 26b** shows that sensor with 10 s of doping time has response values of -0.9, -2.1, -3.9, and -5.4% for the different SO₂F₂ concentrations. The sensor with 20 s of doping time has response values of -1.1, -7.8, -11.5, and -19.1% for the different SO₂F₂ concentrations. The sensor with 40 s doping time has response values for -0.9, -3.0, -7.2, and -10.9% to the different SO₂F₂ concentrations. The sensor sensitivities are shown in **Table 10**. The linear fit function and linear correlation coefficient are shown in **Figure 26b**.

2.2.3.3. Gas-sensing properties of sensors with different amounts of doped Pt for SOF₂ gas

Figure 27 shows that the sensor with 30 s of doping time has a resistance change rates of -1.1, -6.3, -10.0, and -19.1% for SOF₂ gas at 25, 50, 75, and 100 ppm, respectively. **Figure 27b** shows that the sensor with 10 s doping time has response values of -3.2, -8.7, -15.8, and -24.9% for the four SOF₂ concentrations. The sensor with 20 s doping time has response values of -2.0, -8.2, -14.2, and -22.3% for the four SOF₂ concentrations. The sensor with 40 s doping time has response values of -0.8, -2.0, -3.9, and -5.3% to four SOF₂ concentrations. The linear fit function and linear correlation coefficient are shown in **Figure 27b**.

Figure 28 shows a comparison chart for the gas-sensing responses of the four sensors for SO₂, SOF₂, and SO₂F₂ gases at 100 ppm and at their optimal working temperatures. The responses of the intrinsic TiO₂NT sensor for these decomposition gases are discussed in Ref. [30]. With increasing doping amount, the sensor response for SO₂ decreases and follows the trend: intrinsic (-73.5%) > 10 s (-53.3%) > 20 s (-33.9%) > 30 s (-13.8%) > 40 s (-6.7%). When the doping amount increases, the sensor response for SO₂F₂ increases and follows the trend: intrinsic (-4.1%) < 10 s (-5.4%) < 20 s (-19.2%) < 30 s (-50.6%) >> 40 s (-10.9%). The responses of the 10, 20, and 30 s sensors for SOF₂ gas are nearly identical; however, response of the 40 s sensor for SOF₂ dramatically decreases.

Figure 28 shows that the *R*% values of the Pt-doped TiO₂ nanotube for the three SF₆ decomposition gases are negative. This result indicates that the resistance of the Pt-doped TiO₂ nanotube sensor tends to decrease. Based on a known response mechanism, the three measured gases serve as reducing gases or as electron-donating gases. The reaction occurs as follows:

$$R + O_{ads}^- \rightarrow RO_{ads} + e^-$$

where R is the SF₆ decomposition component gas (i.e., SO₂, SOF₂, and SO₂F₂), and O_{ads}⁻ is the adsorbed oxygen ion on the sensor surface.

The results show that the reducing function and electron donating effect of SO₂ gas are the most prominent in the micro-oxidation reduction reaction (i.e., most likely to lose electrons). SO₂ is followed by SOF₂, while SO₂F₂ is the weakest. The selectivity of the sensor is highest for SO₂ gas. Therefore, the order of gas-sensing response of the intrinsic sensor for the three tested gases follows: SO₂ (-74.6%) > SOF₂ (-7.8%) > SO₂F₂ (-5.5%) [34].

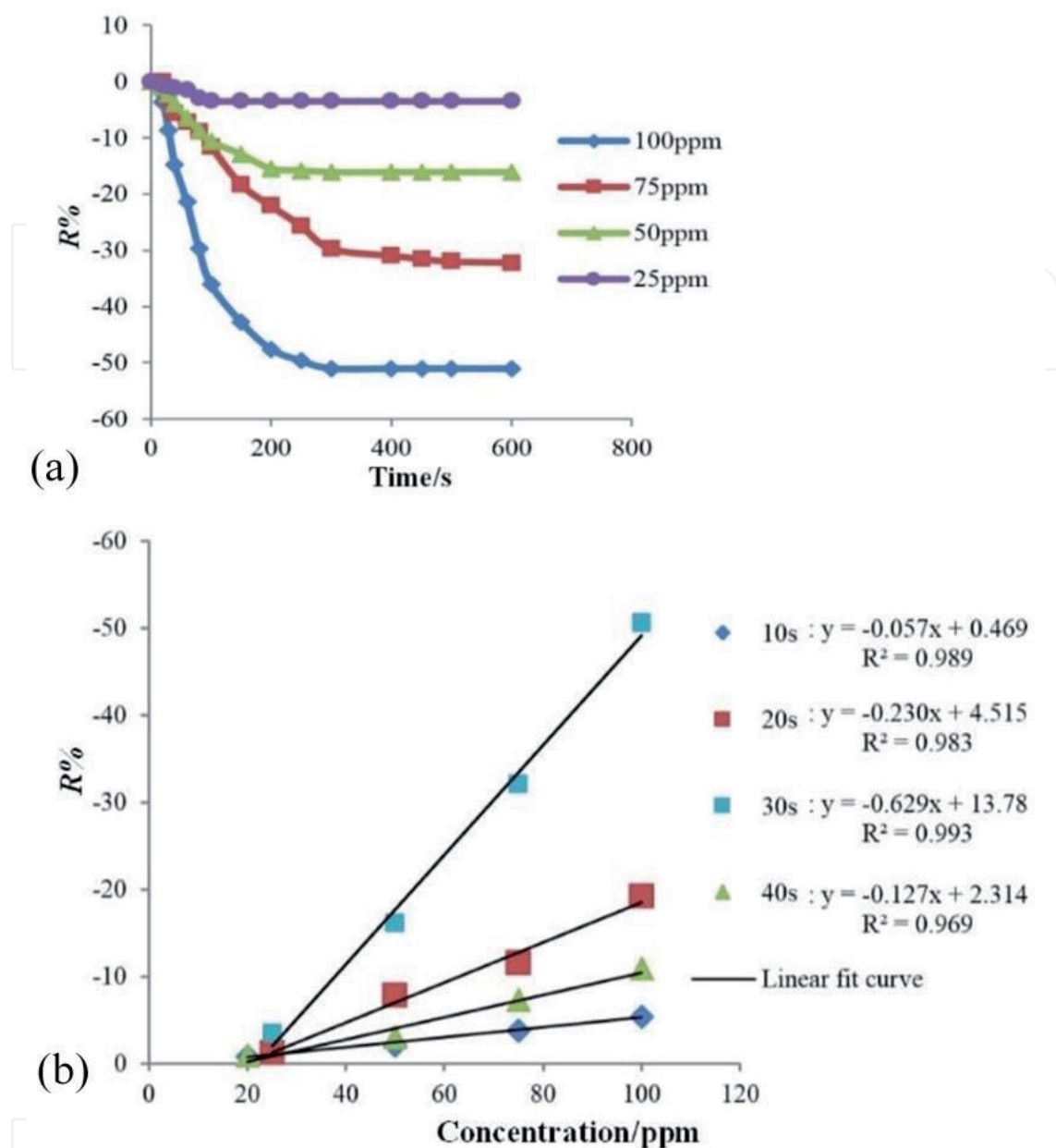


Figure 26. Response of four sensors with different amounts of doped Pt to varying concentrations of SO_2F_2 . (a) Gas-sensing response curves of 30 s sensor for different concentrations of SO_2F_2 gas at 130°C . (b) Linear relationship between sensor response and gas concentration.

Concentration	SO_2F_2			
	10 s	20 s	30 s	40 s
100 ppm	-5.4%	-19.1%	-50.6%	-10.9%
75 ppm	-3.8%	-11.5%	-32.1%	-7.2%
50 ppm	-2.1%	-7.8%	-16.1%	-3.0%
25 ppm	-0.9%	-1.1%	-3.5%	-0.9%

Table 10. Sensitivity of Pt-doped 30 s sensor to different concentrations of SO_2F_2 at optimal working temperature.

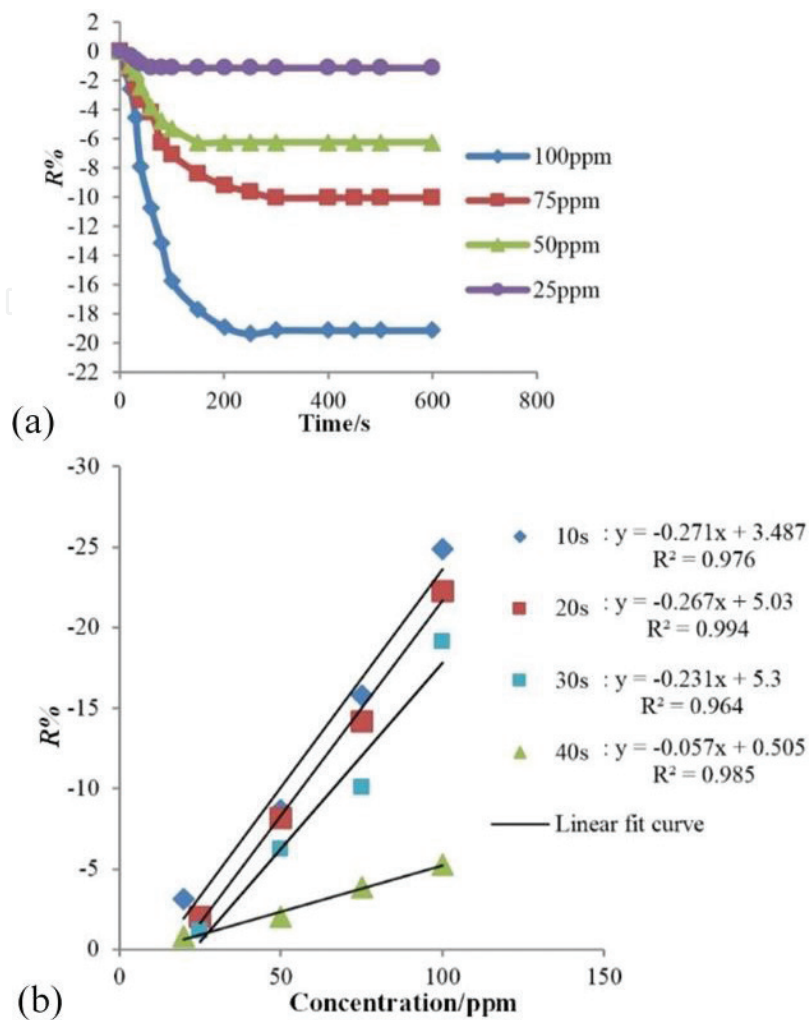


Figure 27. Responses of sensors doped with different amounts of Pt to varying concentrations of SOF₂. (a) Gas-sensing response curves of 30 s sensor for different concentrations SOF₂ gas at 130°C. (b) Linear relationship between sensor response and gas concentration.

The doped Pt significantly affects the gas-sensing response of the TiO₂NT sensor for the SO₂, SOF₂, and SO₂F₂ gases, and thus, the selectivity of the sensor changes.

Pt serves as an oxygen storage point by constantly providing O_{ads}⁻ to the TiO₂NT sensor surface. The noble metal doping specifically reduced the activation energy of the reaction O₂+2e⁻→2O⁻. Thus, the optimal working temperature also decreases, and the reaction rate and gas sensitive effects are enhanced. Meanwhile, the catalyst particles existing on the surface of the TiO₂-sensitive body has better affinity interactions with the target gases. Therefore, these gases will be more attached to the sensor surface at a lower temperature. The catalyst particles are embedded on the surface of the sensitive body. When the adhesion concentration of the measured gas on the catalyst particles surface reaches a certain value, these gases will “overflow” from the catalyst particles toward the surface of the sensitive body, and further react with the adsorbed oxygen ions. Ultimately, the sensitivity of this gas sensor increases, and the sensor response accelerates.

SO₂, SOF₂, and SO₂F₂ gases are specifically discussed. Sulfides have a certain degree of toxicity to noble metal catalysts, and the level of toxicity is associated with the valence elements and

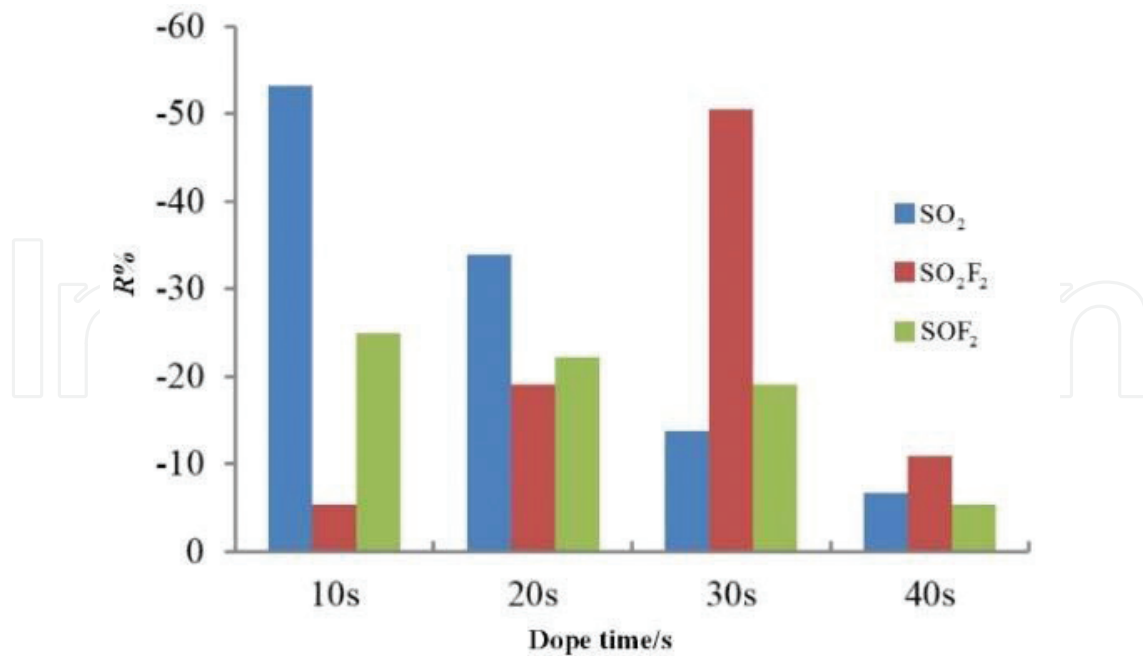


Figure 28. Gas-sensing response of sensor with different amounts of doped Pt to SF₆ decomposition components.

molecular structure. The decreasing toxicity of the three experimental gases follows the order of SO₂ > SOF₂ > SO₂F₂; S⁶⁺ within a certain range is non-toxic [35]. Therefore, once the strong toxicity of SO₂ accumulates, the Pt-doped sensor would be poisoned. The sensor poisoning follows a specific process. First, SO₂ is physically adsorbed on the active center of the catalyst, and then, redox reaction occurs between SO₂ and the active ingredient. Ultimately, the reaction produces alkylene sulfide and other sulfides, which block the active sites. In this complex series of processes, the activity of the catalyst decreases [35]; in addition, the sensitivity of the sensor is significantly improved with the nearly non-toxic SO₂F₂ gas.

2.3. Au-doped TiO₂ nanotubes

2.3.1. Investigation of gas-sensing simulation of Au-doped TiO₂ nanotubes

Intrinsic anatase TiO₂ (101) surface model was optimized in Dmol³ module shown in **Figure 29a, b** while Au-doped anatase TiO₂ (101) surface model after optimization was exhibited in **Figure 29c and d**.

In **Figure 30** [1], density of states (DOS) of intrinsic and Au-doped anatase (101) surfaces as well as the doped Au atom was compared. As can be concluded, Au-doping could reduce band gap of TiO₂, to some extent [1]. To obtain more precise values, highest occupied molecular orbital (HOMO) and lowest unoccupied molecular orbital (LUMO) were calculated, and band gap of Au-doped anatase (101) surface was 1.906 eV, less than 1.932 eV, band gap of intrinsic anatase (101) surface [1]. The decrease of band gap made it easier for electrons to transfer from valence band to conduction band. In addition, Au-doping enhanced the DOS below Fermi level and increased density of electrons, providing more electrons which were possible to transfer to conduction band [1].

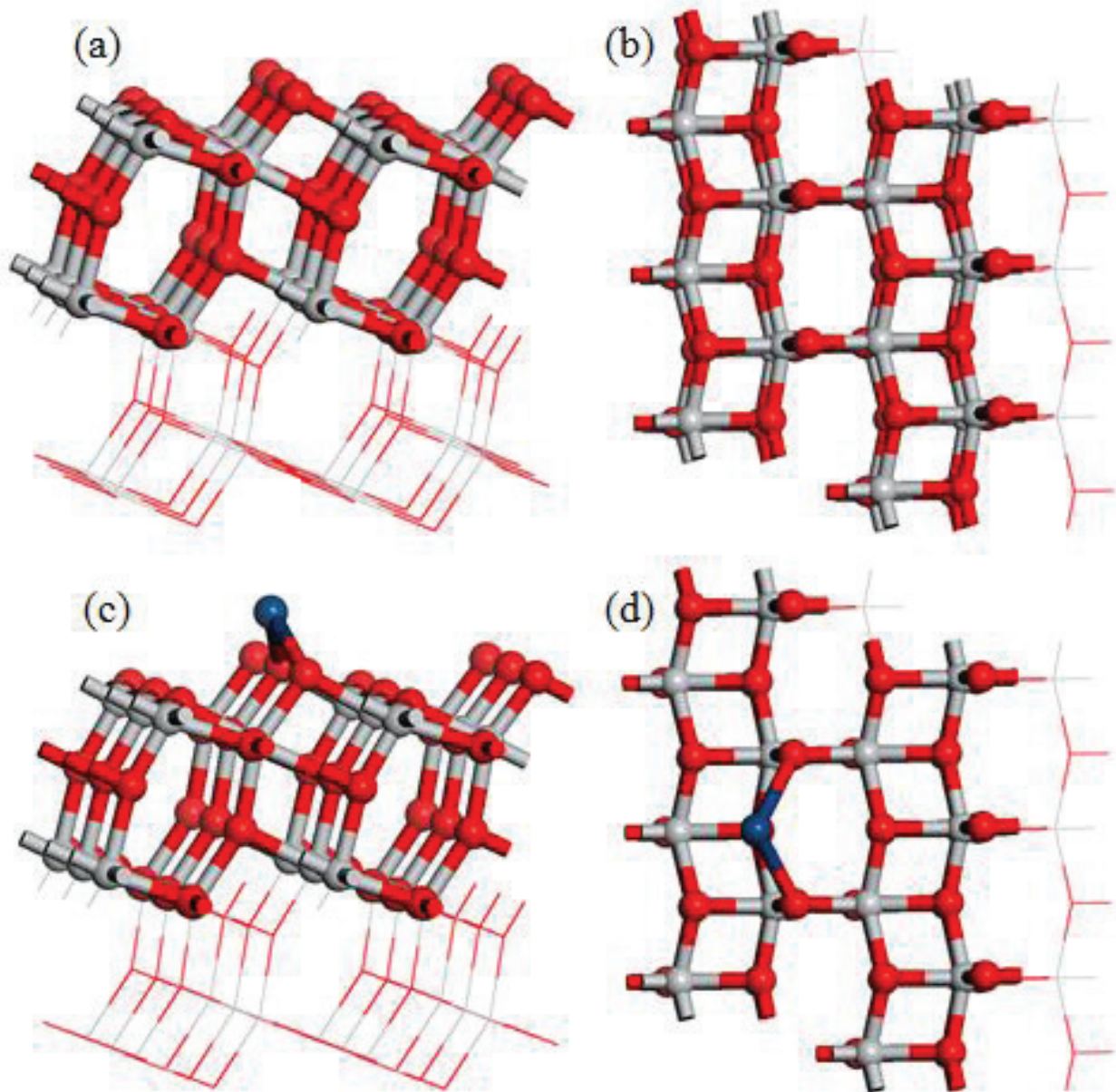


Figure 29. Views of intrinsic and Au-doped anatase TiO₂ (101) surface models from different angles.

Gas molecules approach Au-doped anatase TiO₂ (101) surface by different atoms, shown in **Figure 31**. Considering structure features of SO₂F₂ that S atom is inside the tetrahedron made of O and F atoms, two conditions that SO₂F₂ approaches Au-doped anatase TiO₂ (101) surface by O and F atoms were taken into consideration.

Table 11 [1] shows adsorption parameters of gases adsorbed on Au-doped anatase TiO₂ (101) surface. As can be found, when SO₂ molecule approaches Au atom by O or S atoms, adsorption parameters are close to each other, while similar condition occurs when SOF₂ approaches Au atom. When SO₂F₂ approaches Au atom by O atom, the adsorption energy and charge transfer are obviously smaller than those of the other condition that SO₂F₂ approaches Au atom by F atom, which indicates that it is easier for SO₂F₂ to adsorb on Au atom by F atom.

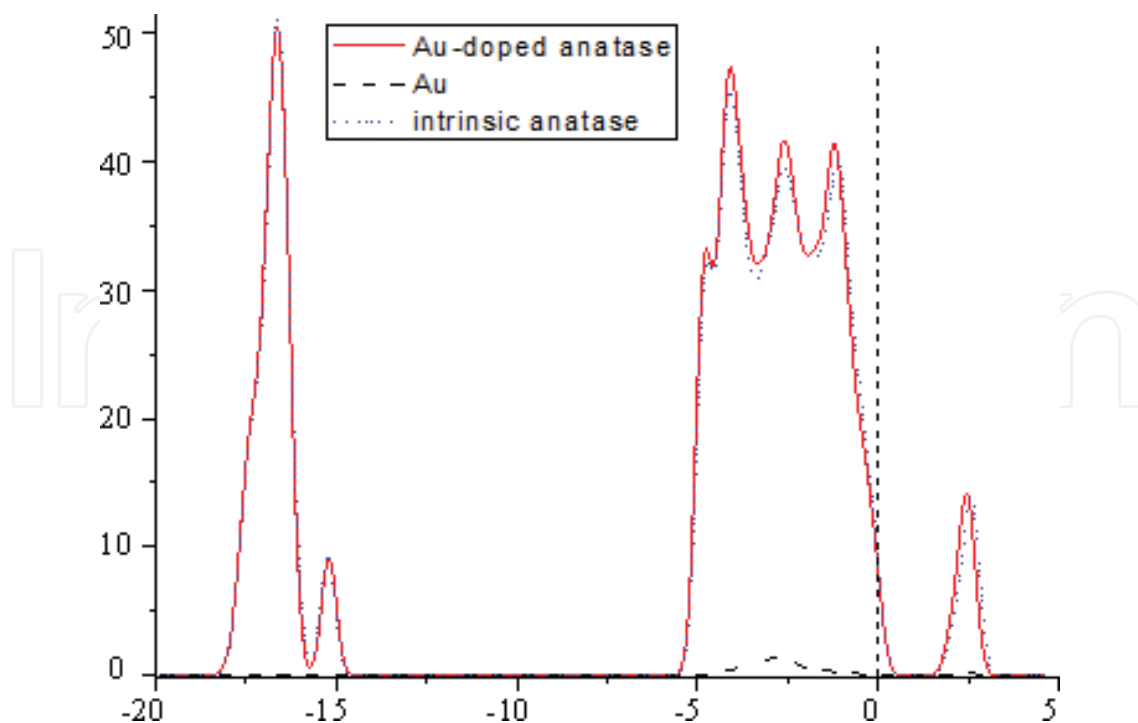


Figure 30. DOS of intrinsic and Au-doped anatase TiO₂ (101) surface.

By comparison of adsorption energy, it can be concluded that, whatever figure gas molecules approach adsorption surface by, adsorption energy of SO₂ is the largest, about 2–3 times that of SOF₂ and SO₂F₂ [1]. It can also be found from the view of charge transfer that, electrons transfer from adsorption surface to SO₂ molecule, the opposite direction of electron transfer in SOF₂ and SO₂F₂ adsorption processes [1]. The phenomenon can be explained by the strong oxidizing ability of SO₂. In addition, SO₂ adsorption possesses larger absolute value of charge transfer in adsorption process than SOF₂ and SO₂F₂ adsorption processes.

Figures 32–34 showed the total density of states (TDOS) of adsorption system and partial density of states (PDOS) of adsorbed gas molecules, SO₂, SOF₂, and SO₂F₂, respectively. “SO₂-O-TiO₂” represents that SO₂ approaches anatase TiO₂ (101) surface by O atom, and the like.

In order to investigate the effect of Au-doping on gas-sensing properties of TiO₂ (101) surface, simulation results were compared with those of gas molecules adsorbed on intrinsic TiO₂ (101) surface [1]. Detailed calculation and results of adsorption on intrinsic TiO₂ (101) surface were included in the published reference [1, 36–39]. It should be noted that, in reference [32], SO₂ and SOF₂ molecules were adsorbed on intrinsic anatase TiO₂ (101) surface by O atom, while SO₂F₂ approached adsorption surface by F atom [1]. Therefore, the comparisons of adsorption parameters are mainly based on calculation results when gas molecules approached surface by the same atom [1]. In this paper, more approaching figures of gas molecules adsorbed on TiO₂ (101) surface are involved [1].

As can be concluded from the adsorption parameters, adsorption energy and charge transfer increased obviously after SO₂ molecule was adsorbed on Au-doped anatase TiO₂ (101) surface

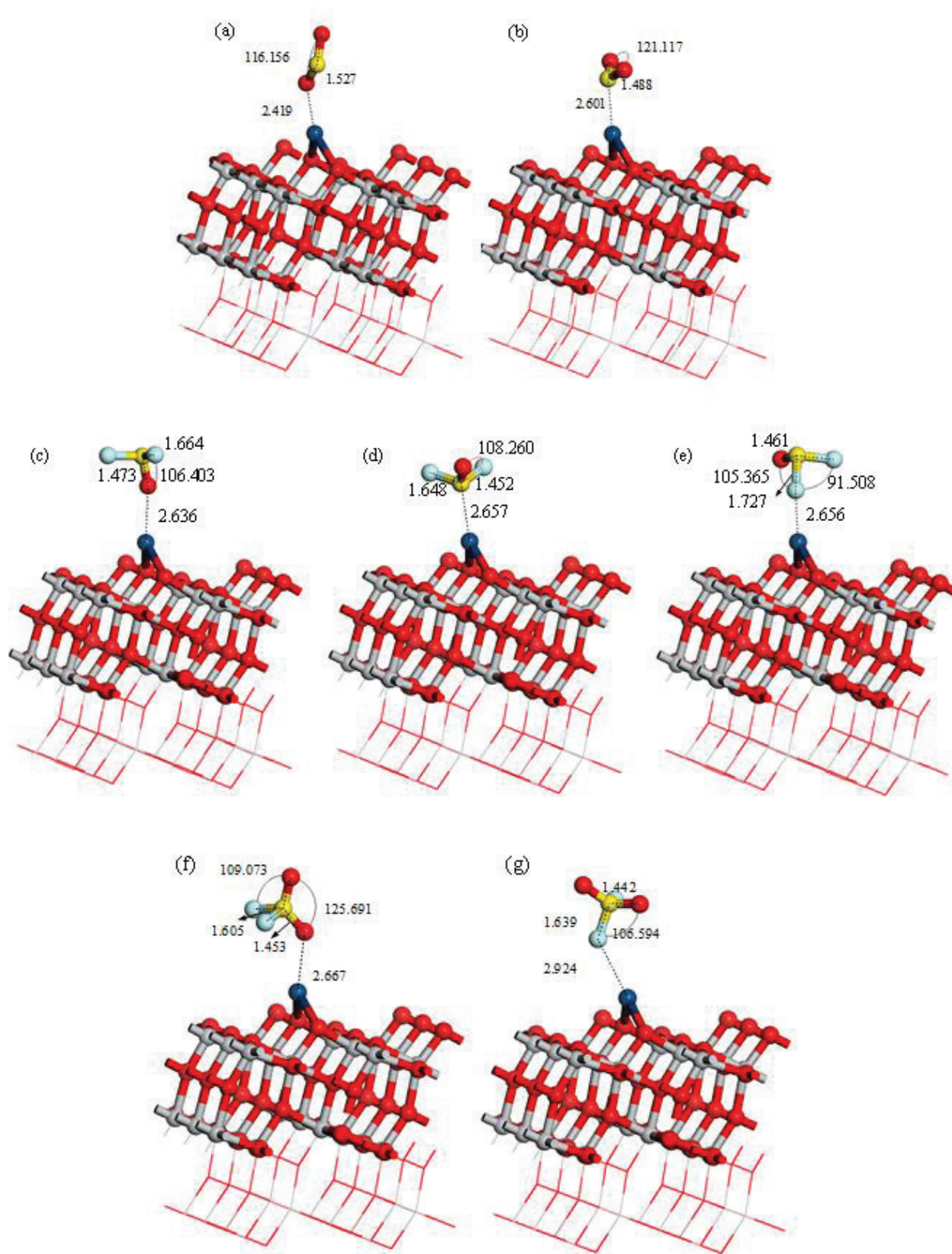


Figure 31. Adsorption structures of three gas molecules on Au-doped anatase TiO₂ (101) surface.

Gas molecules	Adsorption structure	Adsorption energy E_a/eV	Charge transfer Q/e	Adsorption distance $d/\text{Å}$
SO ₂	-S	-0.657	-0.156	2.601
	-O	-0.571	-0.182	2.419
SOF ₂	-S	-0.238	0.067	2.657
	-O	-0.363	0.042	2.636
	-F	-0.593	-0.006	2.656
SO ₂ F ₂	-O	-0.071	0.009	2.667
	-F	-0.200	0.039	2.924

Table 11. Adsorption parameters of gases adsorbed on Au-doped anatase TiO₂ (101) surface “-S”, “-O” and “-F” represent that gas molecules approach adsorption surface by S, O and F atoms, respectively.

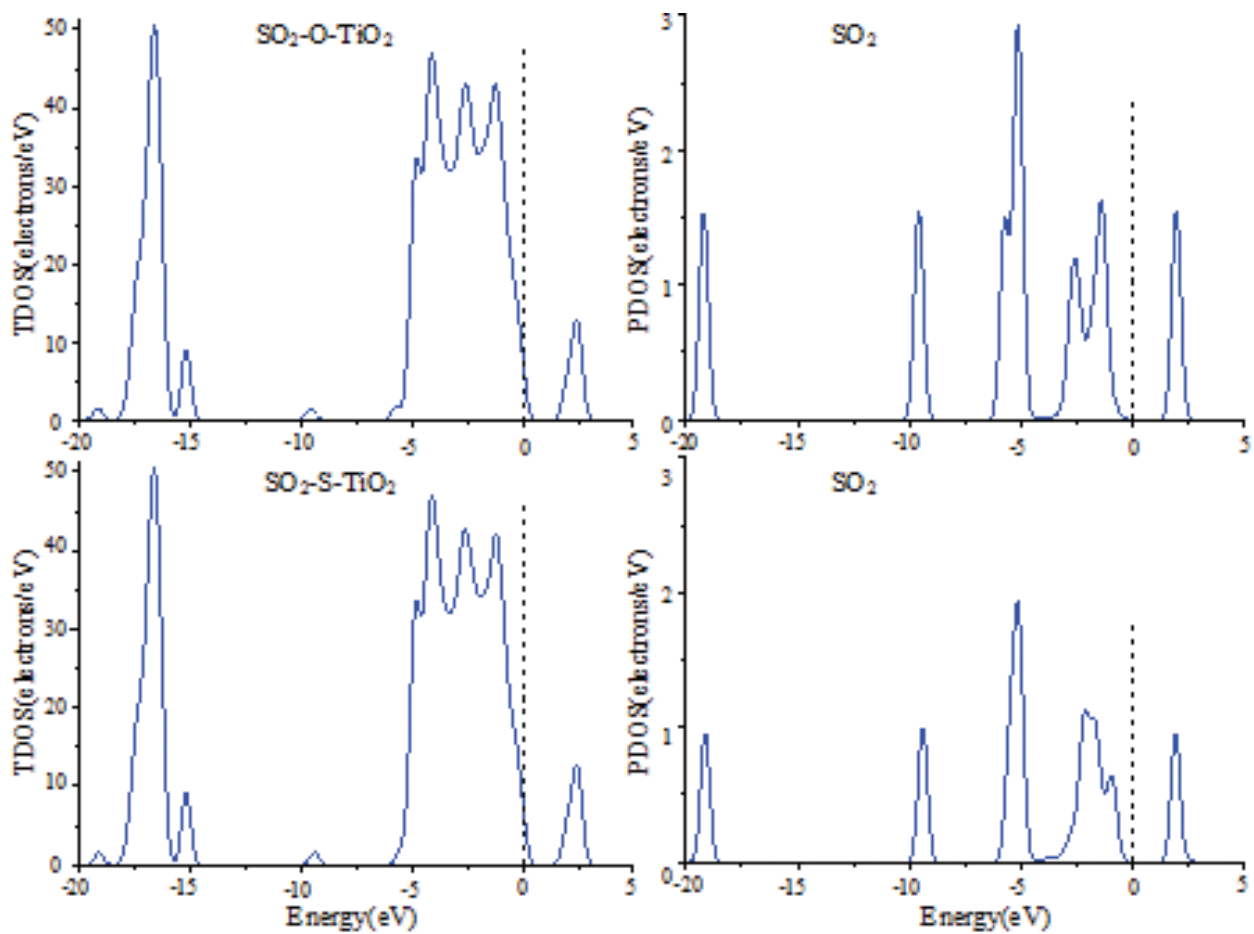


Figure 32. TDOS of adsorption systems and PDOS of adsorbed SO₂.

than intrinsic anatase TiO₂ (101) surface, while adsorption distance changed slightly [1]. More importantly, Au-doping changed the direction of charge transfer, causing the resistivity of adsorption system changing from decrease to increase [1]. As for SOF₂, adsorption energy increased by one-third while charge transfer and adsorption distance kept almost unchanged [1]. It can be judged that adsorption ability of SOF₂ on Au-doped surface slightly increased

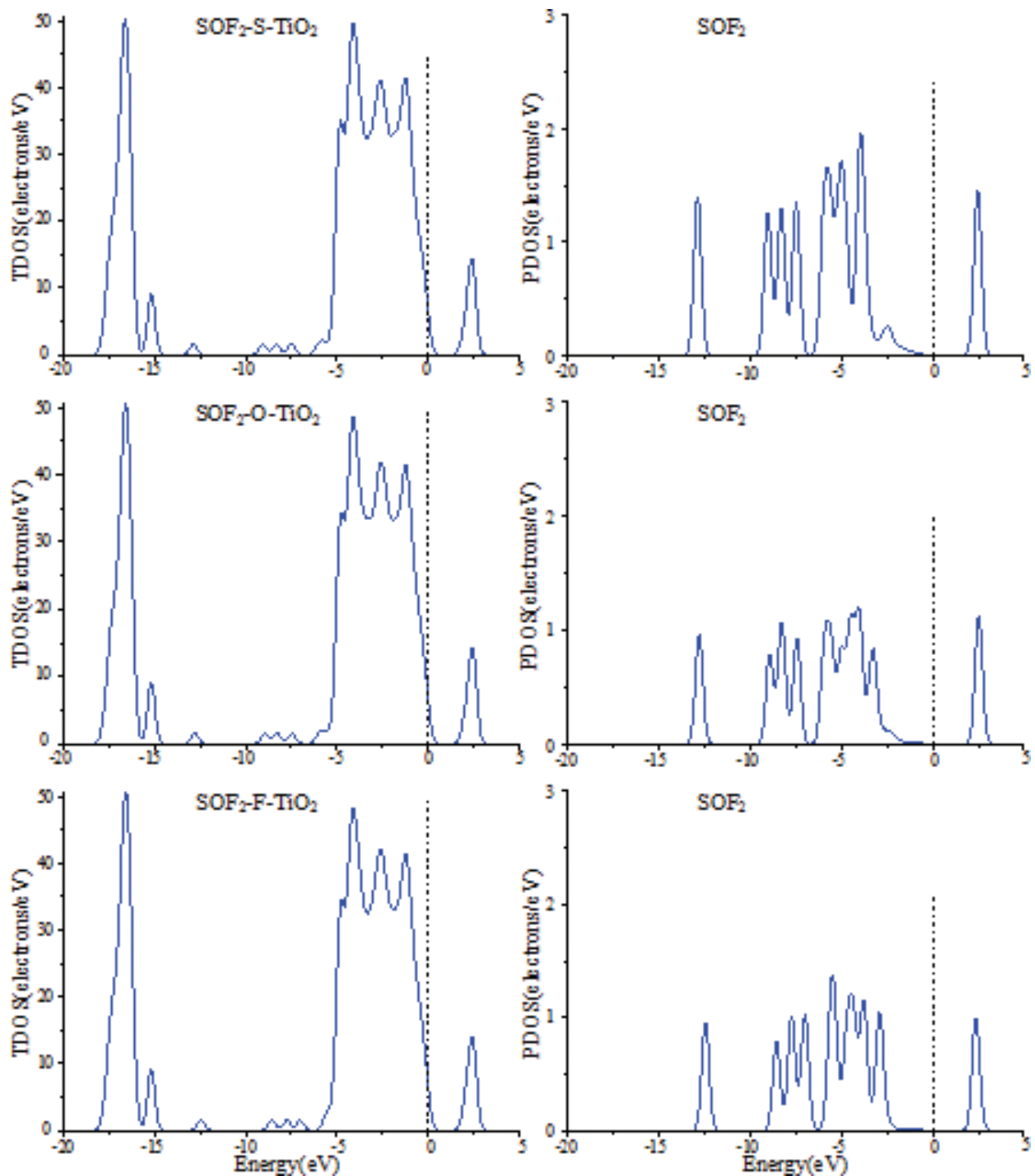


Figure 33. TDOS of adsorption systems and PDOS of adsorbed SOF₂.

compared with that of SOF₂ on intrinsic surface [1]. After SO₂F₂ was adsorbed on Au-doped anatase TiO₂ (101) surface, adsorption distance became smaller, while adsorption energy and charge transfer became larger compared with the adsorption on intrinsic anatase TiO₂ (101) surface. It can also be found that absolute values of adsorption energy and charge transfer became larger when three molecules were adsorbed on Au-doped TiO₂ (101) surface with

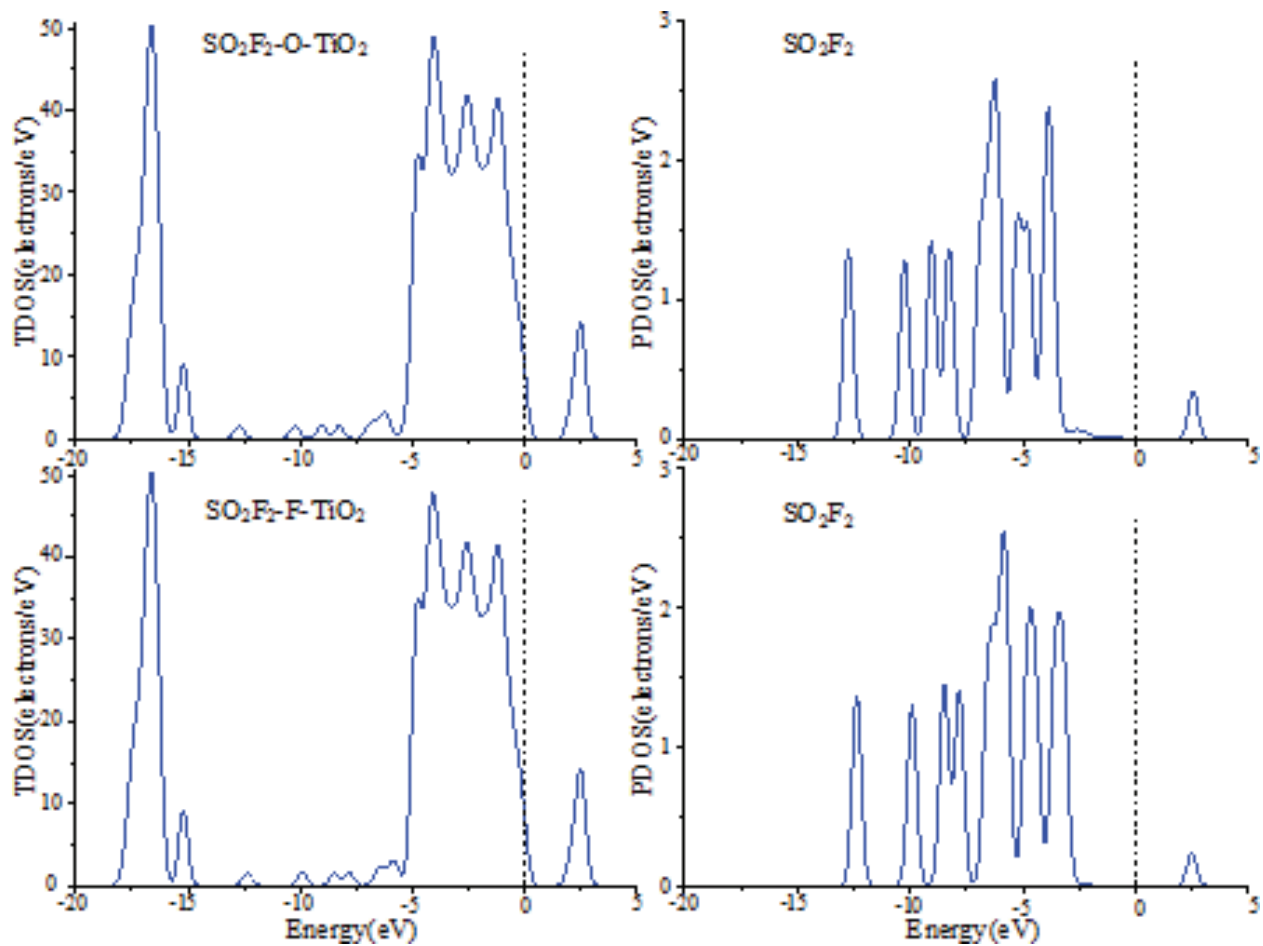


Figure 34. TDOS of adsorption systems and PDOS of adsorbed SO_2F_2 .

adsorption distance almost unchanged compared with the adsorption on intrinsic surface. That is to say, Au-doping improved adsorption performance of intrinsic anatase TiO_2 (101) surface to SO_2 , SOF_2 , and SO_2F_2 [1]. When SO_2 molecule was adsorbed on Au-doped adsorption surface by S atom, adsorption energy was $0.657 > 0.6$ eV, so the process belonged to chemical adsorption, while adsorption energy was 0.571 eV when SO_2 molecule was adsorbed by O atom, slightly smaller than 0.6 eV, which can be considered close to chemical adsorption. Adsorption energies of SOF_2 and SO_2F_2 molecules adsorbed on Au-doped adsorption surface were much smaller than 0.6 eV, belonging to physical adsorption [1].

TDOS of adsorption systems and gas molecules was compared, too [1]. Reference [41] shows TDOS of adsorption systems and PDOS of gas molecules adsorbed on intrinsic anatase TiO_2 (101) surface. By comparing with adsorption on intrinsic anatase TiO_2 (101) surface, an obvious TDOS peak did not appear above Fermi level when SO_2 was adsorbed on Au-doped anatase TiO_2 (101) surface [1]. As can be concluded, SO_2 molecule contributed less electrons to conduction band, leading to increase of adsorption system's resistivity, which is consistent with the above analysis based on adsorption parameters. Au-doping changed variation tendency of adsorption system's resistivity when SO_2 was adsorbed on anatase TiO_2 (101) surface [1].

Compared with adsorption of SOF₂ on intrinsic anatase TiO₂ (101) surface, SOF₂ made obvious contribution to DOS near Fermi level when it was adsorbed on Au-doped anatase TiO₂ (101) surface, which increased the amount of electrons in conduction band. From macroscopic view, resistivity of adsorption system dropped more severely and resistance declined more wildly as well in the adsorption process [1]. That is to say, Au-doping improved the sensitivity of anatase TiO₂ (101) surface to SOF₂, to some extent.

As far as SO₂F₂, adsorption of SO₂F₂ molecule did not contribute much to the DOS near Fermi level when SO₂F₂ was adsorbed on intrinsic anatase TiO₂ (101) surface, that is, SO₂F₂ provided almost no electrons for conduction band of adsorption system [1]. When SO₂F₂ was adsorbed on Au-doped anatase TiO₂ (101) surface, however, obvious DOS peaks appeared above Fermi level, and SO₂F₂ supplied more electrons to conduction band of adsorption system. Macroscopically, sensitivity of Au-doped anatase TiO₂ (101) surface to SO₂F₂ increased obviously compared with intrinsic anatase TiO₂ (101) surface [1].

Based on the above analysis of adsorption parameters and density of states, it can be concluded that, resistance's variation tendency of Au-doped anatase TiO₂ (101) surface after the adsorption of SO₂ is decreasing, different from intrinsic anatase TiO₂ (101) surface [1]. Resistance of Au-doped anatase TiO₂ (101) surface dropped more, and the sensitivity increased slightly after SOF₂ adsorption, while resistance of Au-doped anatase TiO₂ (101) surface dropped severely, and the sensitivity increased obviously after SO₂F₂ adsorption [1].

2.3.2. Preparation and surface characterization of Au-doped TiO₂ nanotubes

To prepare the Au-TNTA, the intrinsic TiO₂ nanotubes were first fabricated, and then, Au was deposited onto the TiO₂ nanotubes using the deposition-precipitation method. The intrinsic TNTAs used in this paper were prepared by the anodic oxidation method [1, 38], and NaOH was selected as the precipitating agent. Firstly, the pH of the 1.01 × 10⁻³ mol/L HAuCl₄ solution was adjusted to 9 using NaOH solution [1]. Then, the intrinsic TiO₂ nanotubes were subsequently added to the above solution, resulting in the pH value decreasing. At the moment, a little more NaOH solution was needed to maintain the pH value at 9. Next, the resulting suspension was stirred for 2 h at 70°C to allow the Au to be supported on the carrier sufficiently. During the process, the suspension became pale purple gradually, and the pH value remained at 9 after cooling. TiO₂ nanotubes were picked out, washed, filtered, dried at room temperature and calcined for 4 h at 100°C to finally obtain the Au-TiO₂ nanotube sensors [1, 39].

As for the reasons for keeping the pH at 9, the selection of a pH value of 8–9 is in agreement with several previous experimental investigations [1, 40–45]. A number of groups have proven that the selection of pH leads to different geometries of TiO₂ [1, 45], and the pH of an aqueous solution dramatically affects the particle size of Au [1, 43]. Though a finite value for the size cannot be deduced from the activity, since the electronic factors depend on the interaction with the support, the morphology of the particle or the chemical state of the gold, there is general agreement that the activity increases as the particle size decreases [1, 44]. Hence, the pH value of the solution has significant influence on the catalytic activity.

A low pH causes a big Au particle, while a high pH causes a low Au deposition amount. The optimum pH aims to not only cause Au to be completely precipitated, but also leads to an appropriate diameter [1, 45]. Ivanova et al. have proven that when the pH value is above 8, the main species of Au in the solution is transformed from AuCl_4^- to $\text{Au}(\text{OH})_4^-$, leading to a smaller particle diameter. In order to remove Cl^- ions completely [1, 46], we chose a pH of 9.

The sample morphology was analyzed by scanning electron microscopy (SEM). The SEM images were obtained by JEOLJSM7000 field emission SEM equipment operated at 10 kV [1].

Figure 35 [1] shows SEM images of the pore size distribution of films composed of (a) intrinsic TiO_2 nanotubes and aggregates and (b) the Au nanoparticles distribution of Au-TiO_2 prepared by the deposition-precipitation method. The surfaces of the films were observed before and after Au deposition [1]. It is obvious that the morphology of the TiO_2 films is significantly changed after the Au nanoparticle modification. The adopted fabrication method results in the formation of tubular TiO_2 of 25 nm in diameter [1]. After the Au deposition treatment, the diameter of the tubes remains about the same. However, on the Au-TiO_2 surface, the pipes are covered with Au nanoparticles of a dozen nanometers in size, aggregating at the pipe orifices [1]. The SEM images confirm that the formed films, whether composed of intrinsic or Au-TiO_2 , are homogeneous with a uniform distribution of pores or Au nanoparticles, respectively, as expected [1].

The crystal structures of the obtained intrinsic TiO_2 and Au-TiO_2 nanotubes were analyzed by X-ray diffraction, measured on an X'pert Pro (PANalytical, The Netherland) using $\text{Cu K}\alpha$ radiation ($\lambda = 0.15405$ nm) at 40 kV, 35 mA. The wide-angle XRD patterns were collected at a scanning speed of $10^\circ/\text{min}$ over the 2θ range of 20° – 100° . **Figure 36** [1] gives the XRD patterns of the products prepared by the deposition-precipitation treatment. Previously, Varghese et al. observed both the anatase and rutile phases of TiO_2 by annealing treatment in ambient oxygen [1, 47, 48]. In our study, the labels A at 25.3° are observed in intrinsic, as well as in Au-doped

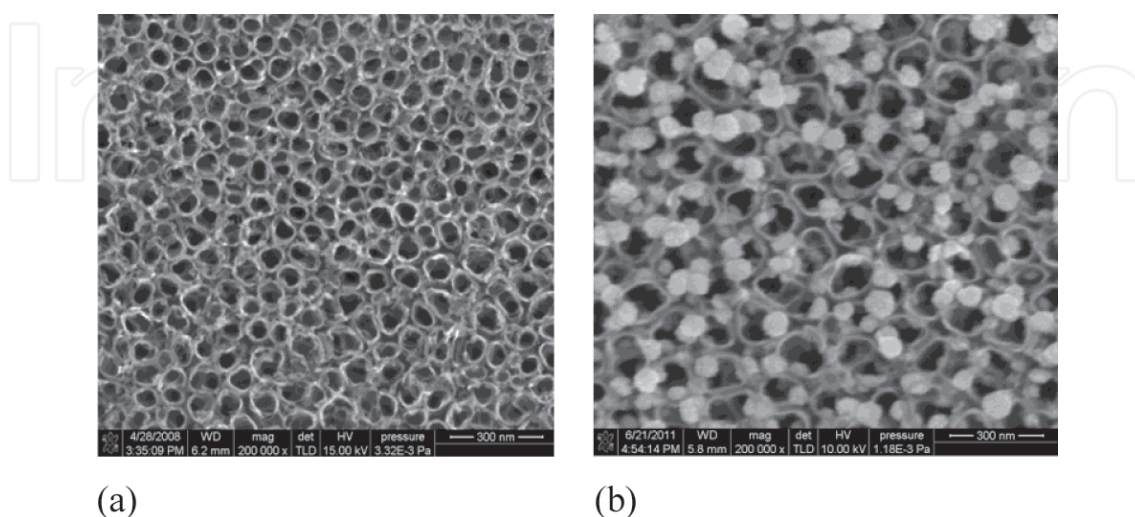


Figure 35. (a) SEM image of the intrinsic TiO_2 nanotubes. (b) SEM image of the Au-TiO_2 nanotubes.

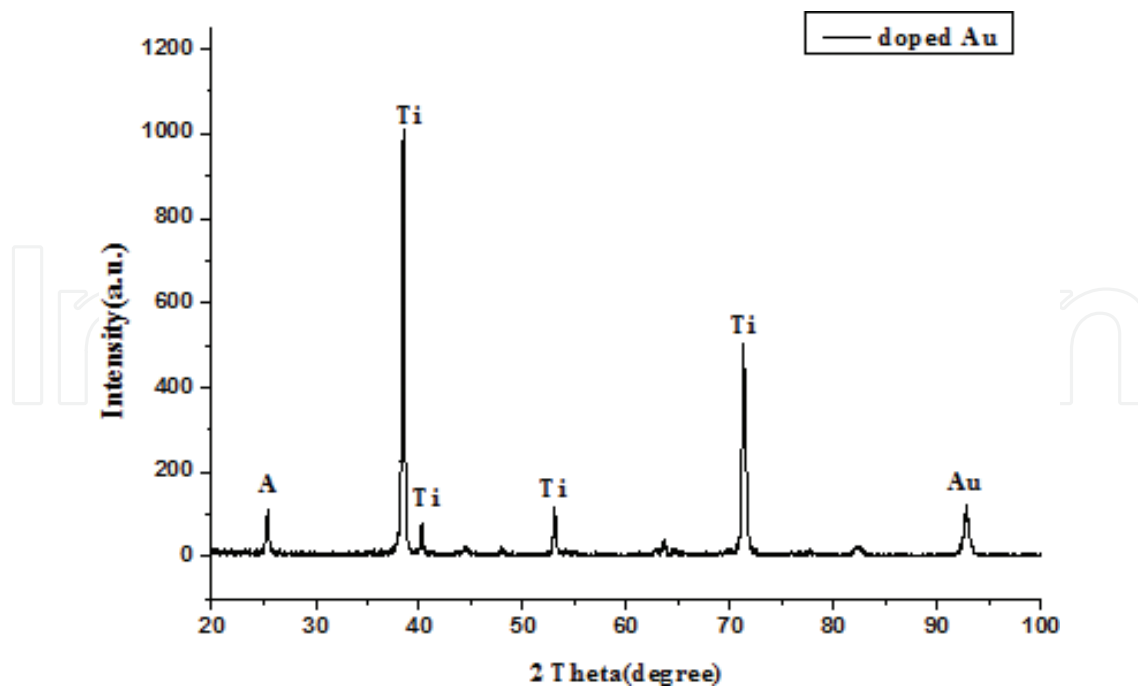


Figure 36. XRD of Au-TiO₂ nanotubes.

TiO₂, indicating that the crystal phases of TiO₂ are both anatase according to previous structural characterizations [1, 49], for which it can be confirmed that, in these preparation conditions, the TiO₂ nanotubes adopt an anatase crystal structure, while a rutile structure is not observed. The labels T and Au represent the reflections from the titanium substrate and different Au crystallographic forms. It is clearly seen from **Figure 36** [1] that characteristic gold peaks come into existence in XRD analysis observed at 38.2° (111), 44.2° (200), 64.3° (220) and 98.1° (400), respectively. The main Au (111) characteristic peak suggests that approximately 10-nm gold nanoparticles are coated onto the anodized TiO₂ nanotubes on the basis of the Scherer formula [1, 50].

Meanwhile, a certain amount of 200, 220 and 400 Au particle crystal forms do exist [1]. There is a popular belief that the characteristics of a metal oxide semiconductor are greatly affected by the doped metal or metalloid, which would also influence the operating temperature in a sensing application further. Therefore, it is necessary to investigate the gas-sensing response of Au-TiO₂ NTAs to SF₆ decomposed components (i.e., 50 ppm SOF₂, SO₂F₂ and SO₂) in an operating range of 20–200°C in order to find out the optimum operating temperature [1].

2.3.3. Gas-sensing experiments of Au-doped TiO₂ nanotubes sensors

Figure 37 [1] depicts the curves of the resistance changes' rate (i.e., the response value) of Au-doped and intrinsic TiO₂ NTAs to SO₂, SOF₂ and SO₂F₂ at different operating temperatures. The response value of the intrinsic TiO₂ nanotubes to SF₆ decomposed components increases as the surface temperature rises, reaching saturation around 180°C, which is considered the optimum operating temperature. In the case of Au-TiO₂, the resistance response

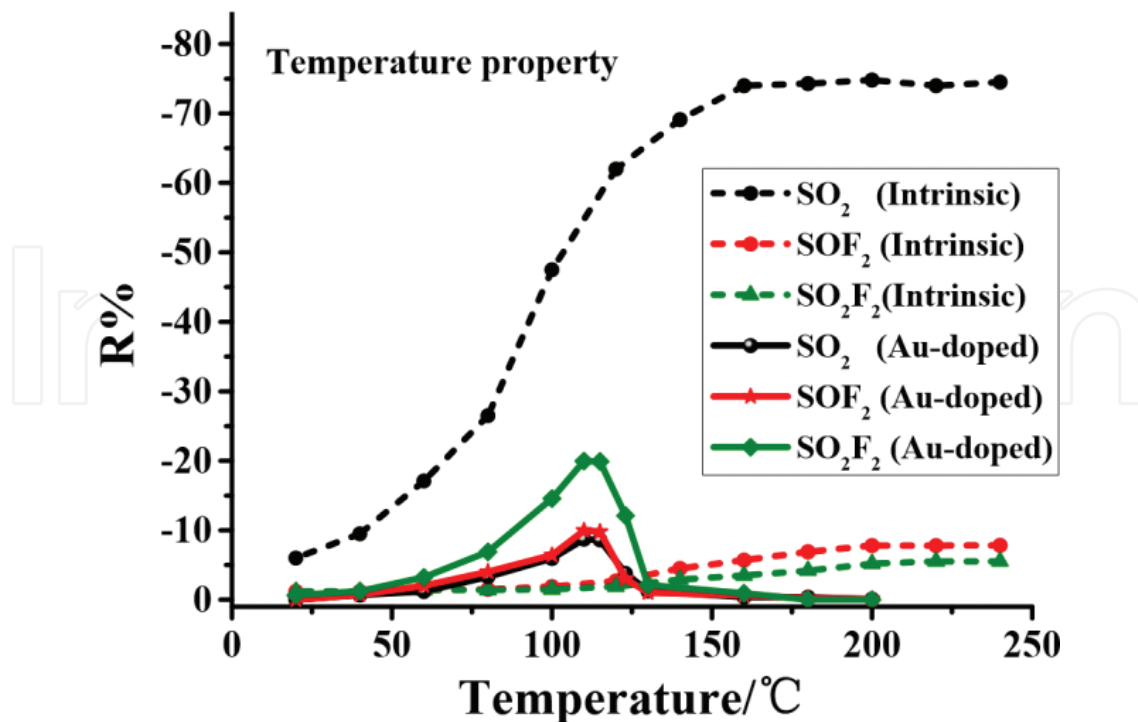


Figure 37. Sensor responses for 50 ppm SO₂ (black dots), SOF₂ (red dots) and SO₂F₂ (green dots), respectively, for the intrinsic (short dashed lines, in the range of 20–240°C) and Au-doped TiO₂ (solid lines, in the range of 20–200°C) nanotubular films at different working temperatures.

increases with increasing operating temperature before 110°C, following the typical behavior of an oxide semiconductor [1]. However, the resistance response dramatically drops down when the temperature exceeds 110°C. Hence, the optimum operating temperature of the Au-TiO₂ nanotubes sensor is taken as 110°C. A comparison of Au-doped and intrinsic TiO₂ indicates that Au-doping reduces the working temperature of TiO₂ NTAs along with obvious changes in the temperature characteristic curve [1].

The performance of the intrinsic TiO₂ nanotube sensors maintaining its response value after it reaches 180°C might be attributed to the dynamic equilibrium of the gas adsorption and desorption rate on the sensor's surface in the meantime [1]. As for Au-TiO₂, the Au nanoparticles change the microscopic structure and charge distribution of the surface, and the doped Au results in a promoted chemical desorption rate when the temperature surpasses 110°C, causing the oxygen desorption rate to be faster than its adsorption rate [1]. As a result, the oxygen chemisorption density on the surface decreases, leading to a rapid drop of the response value [1, 51].

The gas-sensing response curves of SO₂, SOF₂ and SO₂F₂ for Au-TiO₂ NTAs were recorded at different concentrations (i.e., 25, 50, 75, 100 ppm) under the optimal operating temperature (110°C) [1]. The results were linearly fit to investigate the linear relationship between the sensor's resistance change and the gas concentration. Therefore, the concentration of target gases in real power equipment could be estimated through the linear relationship acquired by these sample gases [1].

2.3.3.1. Sensing performances of Au-TiO₂ NTAs for SO₂

As **Figure 38** [1] shows, the resistance change rates of the Au-TiO₂ nanotube gas sensor for SO₂ at 25, 50, 75 and 100 ppm are -2.14, -8.73, -15.76 and -23.75%, respectively. The linear

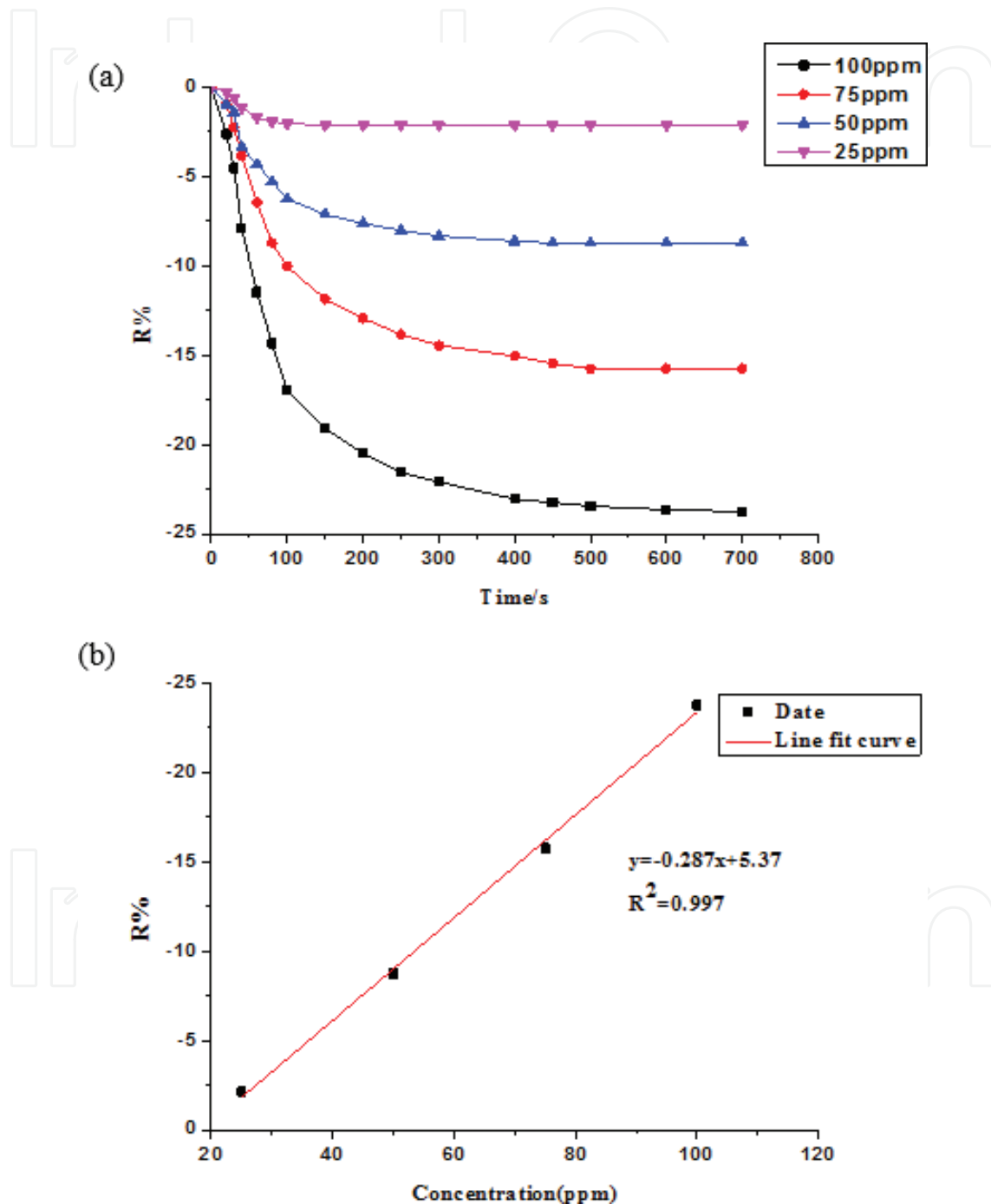


Figure 38. (a) Au-TiO₂ NTAs' response to different concentrations of SO₂ at the 110°C working temperature. (b) Linear relationship between the sensor's response value and the SO₂ concentration.

relationship between the sensor's resistance change rate and the SO₂ concentration is fitted as $y = -0.287x + 5.37$ with a linear correlation coefficient (R^2) of 0.997 [1].

2.3.3.2. Sensing performances of Au-TiO₂ NTAs for SOF₂

Figure 39 [1] exhibits the sensing response curves of the Au-TiO₂ nanotube sensor for SOF₂ at different concentrations under 110°C. From **Figure 39a**, the resistance change rates that correspond to 25, 50, 75 and 100 ppm of SOF₂ are separately -3.00, -9.97, -18.42 and -28.37%. After linear fitting, the linear function is calculated to be $y = -0.338x + 6.197$, as shown in **Figure 39b**,

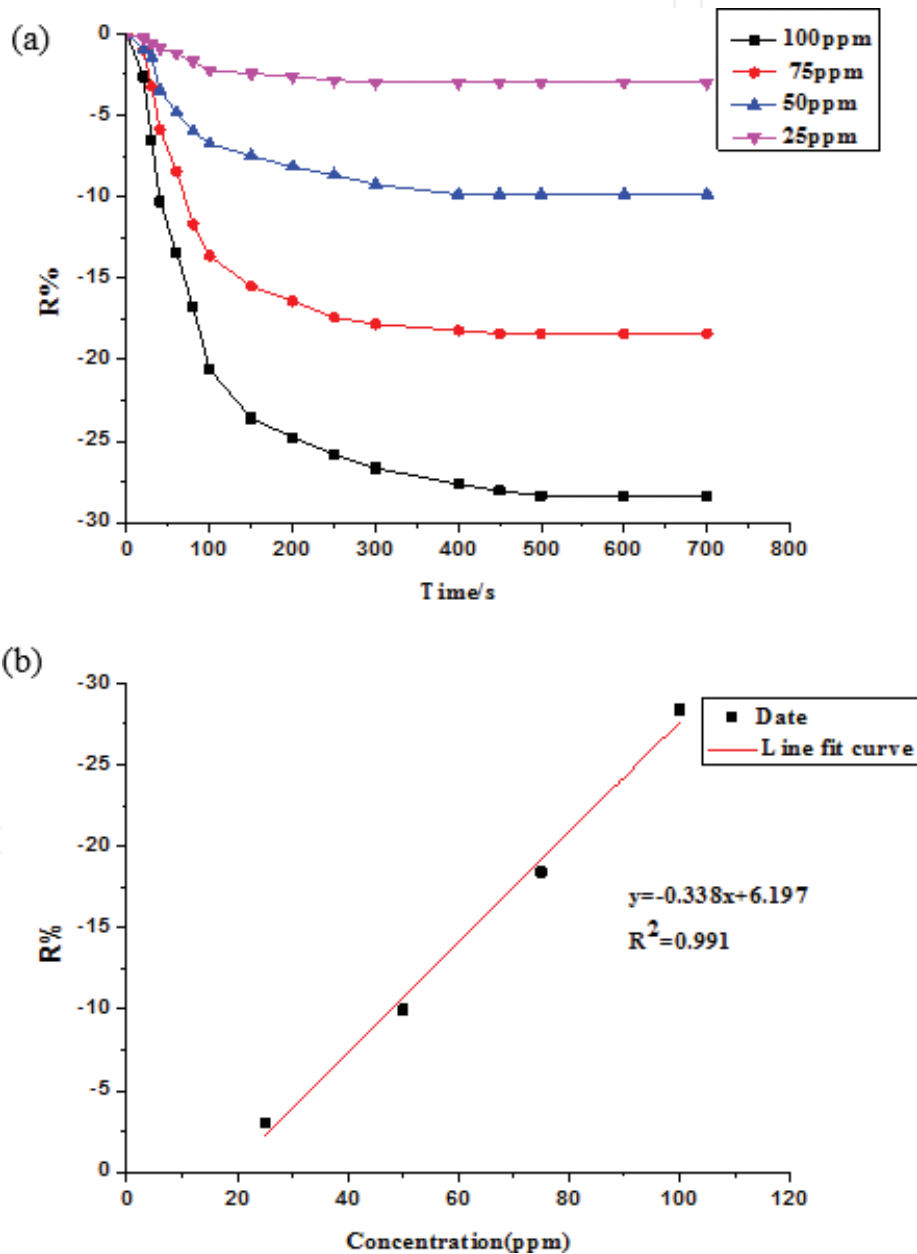


Figure 39. (a) Au-doped TiO₂ NTAs' response to different concentrations of SOF₂ at the 110°C working temperature. (b) Linear relationship between the sensor's response value and the SOF₂ concentration.

with R^2 equaling 0.991. It can be concluded that, within a certain range of concentrations, a linear relationship between the resistance change rate of the Au-TiO₂ nanotube sensor and the SOF₂ concentration is also displayed [1].

2.3.3.3. Sensing performances of Au-TiO₂ NTAs for SO₂F₂

Resistance change rates of Au-TiO₂ nanotube gas sensor for SOF₂ with different concentrations at 25, 50, 75 and 100 ppm are, respectively, -4.04, -19.58, -30.93 and -42.31%, as shown in **Figure 40a**. The linear fitting relationship is $y = -0.503x + 7.138$ and the linear correlation coefficient R^2 equals 0.991 [1].

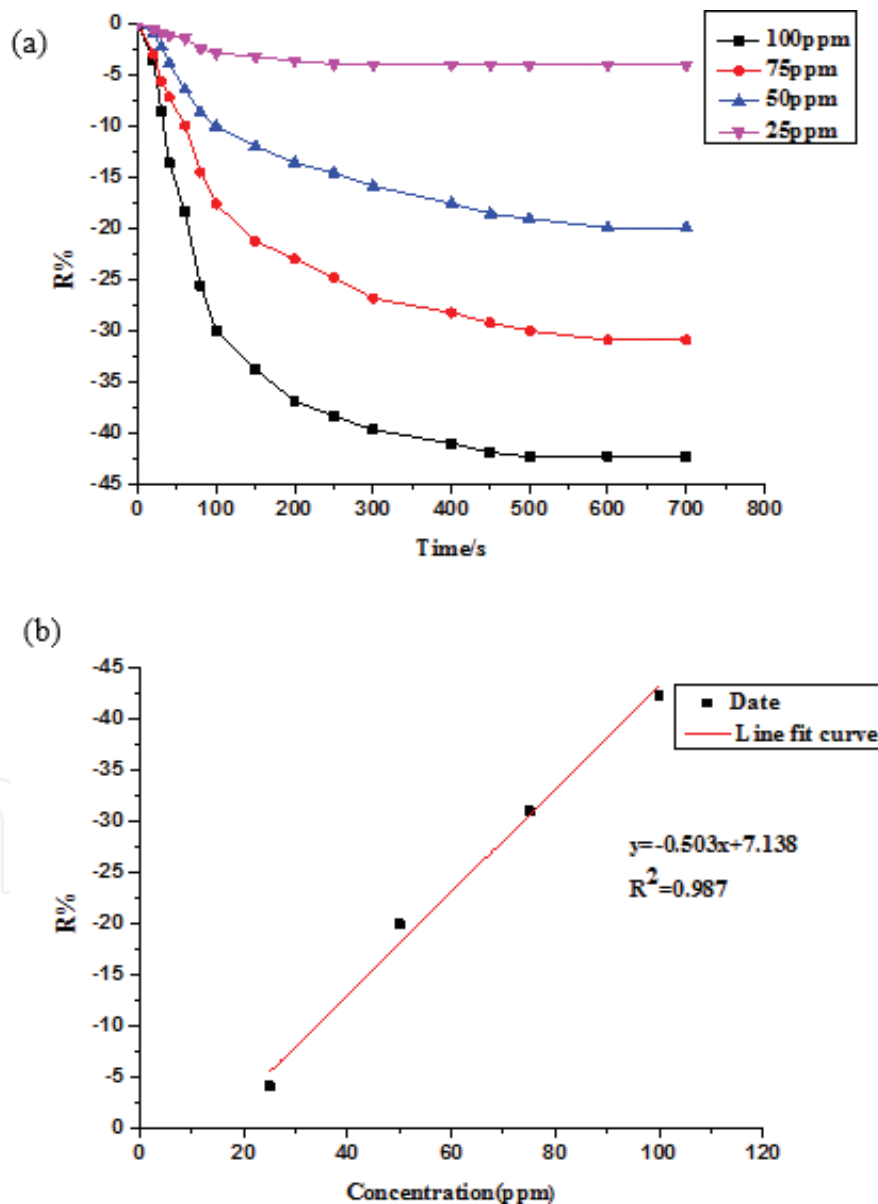


Figure 40. (a) Au-doped TiO₂ NTAs response to different concentrations of SO₂F₂ at the 110°C working temperature. (b) Linear relationship between the sensor's response value and the SO₂F₂ concentration.

Figure 41 [1] shows the gas-sensing response comparison chart of intrinsic and Au-doped TiO₂ NTAs at their optimum operating temperatures for 50 ppm SF₆ decomposed gases, that is, SO₂, SOF₂ and SO₂F₂, where the gas-sensing properties of intrinsic TiO₂ NTAs have been discussed in [1, 52]. The responses of intrinsic and Au-doped TiO₂ NTAs both exhibit a negative behavior, that is, the resistances of intrinsic and Au-doped TiO₂ NTAs decrease after introducing these gases.

The gas-sensing response values of the intrinsic TiO₂ nanotube sensor are SO₂ (-74.6%) > SOF₂ (-7.82%) > SO₂F₂ (-5.52%), while for the Au-TiO₂ nanotube sensor is SO₂F₂ (-19.95%) > SOF₂ (-9.97%) > SO₂ (-8.73%). It is worth noting that the experimental results in our study are statistically significant, the values of which are at the average level according to dozens of experiments [1]. Obviously, the response value of SO₂F₂ dramatically increases, while SO₂ is reduced, and the response of SOF₂ remains constant. The selective detection of SO₂F₂ was actually achieved in our experimental research by the modification of Au nanoparticles at the appropriate operation temperature [1]. Hence, the Au-TiO₂ NTAs are potential substrates for the SO₂F₂ detection application. Furthermore, combined Au-doped and intrinsic TiO₂ arrays are promising substrates for SF₆ decomposition component detection [1].

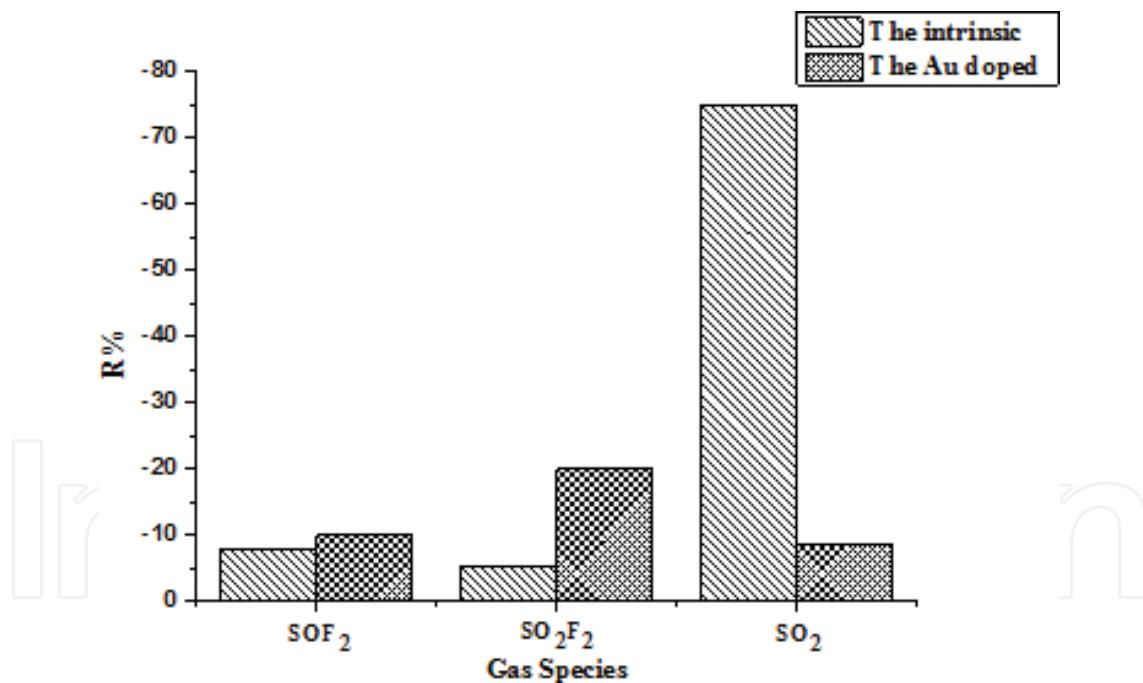


Figure 41. Sensor responses of Au-doped and intrinsic TNTA for SF₆ decomposition components.

Acknowledgements

Parts of this chapter are reproduced from Refs. [27–28] with Elsevier's permission and from Refs. [1, 37] under the terms of their respective Creative Commons licenses.

Author details

Ju Tang, Xiaoxing Zhang*, Song Xiao and Fuping Zeng

*Address all correspondence to: xiaoxing.zhang@outlook.com

School of Electrical Engineering, Wuhan University, Wuhan, China

References

- [1] Xiaoxing Zhang JZ, Yichao Jia, Peng Xiao, Ju Tang. TiO₂ Nanotube Array Sensor for Detecting the SF₆ Decomposition Product SO₂. *Sensors*. 2012;**12**:3302–3313
- [2] Beyer C, Jenett H, Klockow D. Influence of reactive SF_x gases on electrode surfaces after electrical discharges under SF₆ atmosphere. *IEEE Transactions on Dielectrics and Electrical Insulation*. 2000;**7**:234–240
- [3] Mor GK, Shankar K, Paulose M, Varghese OK, Grimes CA. Enhanced photocleavage of water using Titania nanotube arrays. *Nano Letters*. 2005;**5**:191–195
- [4] Grimes CA, Mor GK. *TiO₂ NT Arrays Synthesis, Properties, and Applications*. Norwell, MA: Springer; 2009
- [5] Seo M-H, Yuasa M, Kida T, Huh J-S, Yamazoe N, Shimano K. Detection of organic gases using TiO₂ nanotube-based gas sensors. *Procedia Chemistry*. 2009;**1**:192–195
- [6] Lin S, Li D, Wu J, Li X, Akbar SA. A selective room temperature formaldehyde gas sensor using TNTA. *Sensors and Actuators B*. 2011;**156**:505–509
- [7] Yun H. *Preparation of NO₂ Gas Sensor Based on TiO₂ Nanotubes*. [thesis], Dalian, China: Dalian University of Technology; 2005
- [8] Varghese OK, Gong D, Paulose M, Ong KG, Grimes CA. Hydrogen sensing using Titania nanotubes. *Sensors and Actuators B*. 2003;**93**:338–344
- [9] Mor GK, Varghese OK, Paulose M, Shankar K, Grimes CA. A review on highly ordered, vertically oriented TNTA: Fabrication, material properties, and solar energy applications. *Solar Energy Materials and Solar Cells*. 2006;**90**:2011–2075
- [10] Mor GK, Varghese OK, Paulose M, et al. A review on highly ordered, vertically oriented TNTA: Fabrication, material properties, and solar energy applications. *Solar Energy Materials & Solar Cells*. 2006;**90**(14):2011–2075
- [11] Hulthen JC, Martin CR. A general template-based method for the preparation of nano-materials. *Journal of Materials Chemistry*. 1997;**7**(7):1075–1087
- [12] Lakshmi BB, Dorhout PK, Martin CR. Sol-gel template synthesis of semiconductor nano-structures. *Chemistry of Materials*. 1997;**9**:857–862

- [13] Lakshmi BB, Patrissi CJ, Martin CR. Sol-gel template synthesis of semiconductor oxide micro-and nanostructures. *Chemistry of Materials*. 1997; **9**:2544–2550.
- [14] Gong D, Grimes CA, Varghese OK, et al. Titanium oxide nanotube arrays prepared by anodic oxidation. *Journal of Materials Research*. 2001;**16**:3331
- [15] Kasu G, Hiramata T, Hosono A, et al. Formation of titanium oxide nanotube. *Langmuir*. 1998;**14**:3160
- [16] Cheng ZJ, Liu TY, Yang CX, Gan HX, Chen JY, Zhang FW. Ab initio atomic thermodynamics investigation on oxygen defects in the anatase TiO₂. *Journal of Alloys and Compounds*. 2013;**546**:246–252
- [17] Vittadini A, Casarin M, Selloni A. Chemistry of and on TiO₂-anatase surfaces by DFT calculations: A partial review. *Theoretical Chemistry Accounts*. 2007;**117**:663–671
- [18] Perdew JP, Burke K, Ernzerhof M. Generalized gradient approximation made simple. *Physical Review Letters*. 1996;**77**:3865
- [19] Delley B. An all-electron numerical method for solving the local density functional for polyatomic molecules. *The Journal of Chemical Physics*. 1990;**92**:508–517
- [20] Delley B. From molecules to solids with the DMol approach. *The Journal of Chemical Physics*. 2000;**113**:7756–7764
- [21] Monkhorst H, Pack JD. Special points for Brillouin-zone integrations. *Physical Review B*. 1976;**13**:5188–5192
- [22] Long R, Dai Y, Huang B.B. Energetic and electronic properties of X-(Si, Ge, Sn, Pb) doped TiO₂ from first-principles. *Computational Materials Science*. 2009;**45**:223–228
- [23] Yen CC, Wang DY, Chang LS, Shih HC. Characterization and photocatalytic activity of Fe-and N-co-deposited TiO₂ and first-principles study for electronic structure. *Journal of Solid State Chemistry*. 2011;**184**:2053–2060
- [24] Burdett JK, Hughbanks T, Miller GJ, Richardson JW Jr, Smith JV. Structural-electronic relationships in inorganic solids: powder neutron diffraction studies of the rutile and anatase polymorphs of titanium dioxide at 15 and 295K. *Journal of the American Chemical Society*. 1987;**109**:3639–3646
- [25] Valentin CD, Pacchioni G, Selloni A, Livraghi S, Giamello E. Characterization of paramagnetic species in N-doped TiO₂ powders by EPR spectroscopy and DFT calculations. *The Journal of Physical Chemistry B*. 2005;**109**:11414–11419
- [26] Zhang X, Chen Q, Tang J, Hu W, Zhang J. Adsorption of SF₆ decomposed gas on anatase (101) and (001) surfaces with oxygen defect: a density functional theory study. *Scientific Reports*. 2014;**4**:4762
- [27] Zhang X, Chen Q, Hu W, Zhang J. Adsorptions of SO₂, SOF₂, and SO₂F₂ on Pt-modified anatase (1 0 1) surface: sensing mechanism study. *Applied Surface Science*. 2015;**353**:662–669

- [28] Zhang X, Dong X, Gui Y. Theoretical and experimental study on competitive adsorption of SF₆ decomposed components on Au-modified anatase (101) surface. *Applied Surface Science*. 2016;**387**:437–445
- [29] Zhang X, Chen Q, Hu W, Zhang J. A DFT study of SF₆ decomposed gas adsorption on an anatase (101) surface. *Applied Surface Science*. 2013;**286**:47–53
- [30] Zhang X, Chen Q, Tang J, Hu W, Zhang J. Adsorption of SF₆ decomposed gas on anatase (101) and (001) surfaces with oxygen defect: a density functional theory study. *Scientific Reports*. 2014;**4**:1–11
- [31] Gong D, Grimes CA, Varghese OK, Hu WC, Singh RS, Chen Z, Dickey EC. Titanium oxide nanotube arrays prepared by anodic oxidation. *Journal of Materials Research*. 2001;**16**:3331–3334
- [32] Zhou WQ, Zhai CY, Du YK, Xu JK, Yang P. Electrochemical fabrication of novel platinum-poly(5-nitroindole) composite catalyst and its application for methanol oxidation in alkaline medium. *International Journal of Hydrogen Energy*. 2009;**34**:9316–9323
- [33] Gangal ND, Gupta NM, Lyer RM. Microcalorimetric study of the interaction of CO, O₂, and CO + O₂ with Pt/SnO₂ and SO₂ catalysts. *Journal of Catalysis*. 1990;**11**:13–25
- [34] Zhang XX, Zhang JB, Jia YC, Xiao P, Tang J. TiO₂ nanotube array sensor for detecting the SF₆ decomposition product SO₂. *Sensors*. 2012;**12**:3302–3313
- [35] Okazaki K, Ichikawa S, Maeda Y, Haruta M, Kohyama M. Electronic structures of Au supported on TiO₂. *Applied Catalysis A General*. 2005;**291**:45–54
- [36] Zhang X, Chen Q, Hu W, et al. A DFT study of SF₆ decomposed gas adsorption on an anatase (101) surface. *Applied Surface Science*. 2013;**286**(12):47–53
- [37] Zhang X, Yu L, Jing T, Dong X. Gas sensitivity and sensing mechanism studies on Au-doped TiO₂ nanotube arrays for detecting SF₆ decomposed components. *Sensors*. 2013;**14**:19517–19532
- [38] Xing XZ, Bin JZ, Jia Y, Peng X, Ju T. TiO₂ nanotube array sensor for detecting the SF₆ decomposition product SO₂. *Sensors*. 2012;**12**:3302–3313
- [39] Zhu B, Guo Q, Huang X, Wang S, Zhang S, Wu S, Huang W. Characterization and catalytic performance of TiO₂ nanotubes-supported gold and copper particles. *Journal of Molecular Catalysis A: Chemical*. 2006;**249**:211–217
- [40] Cunningham DAH, Vogel W, Kageyama H, Tsubota S, Haruta M. The relationship between the structure and activity of nanometer size gold when supported on Mg(OH)₂. *Journal of Catalysis*. 1998;**177**:1–10
- [41] Dekkers MAP, Lippits MJ, Nieuwenhuys BE. Supported gold/MO_x catalysts for NO/H₂ and CO/O₂ reactions. *Catalysis Today*. 1999;**54**:381–390
- [42] Macak JM, Schmuki P. Anodic growth of self-organized anodic TiO₂ nanotubes in viscous electrolytes. *Electrochimica Acta*. 2006;**52**:1258–1264

- [43] Xu Q, Kharas KC, Datye AK. The preparation of highly dispersed Au/Al₂O₃ by aqueous impregnation. *Catalysis Letters*. 2003;**85**:229–235
- [44] Gucci L, Beck A, Pászti Z. Gold catalysis: effect of particle size on reactivity towards various substrates. *Catalysis Today*. 2012;**181**:26–32
- [45] Ivanova S, Petit C, Pitchon V. A new preparation method for the formation of gold nanoparticles on an oxide support. *Applied Catalysis A: General*. 2004;**267**:191–201
- [46] Haruta M, Ueda A, Tsubota S, Torres Sanchez RM. Low-temperature catalytic combustion of methanol and its decomposed derivatives over supported gold catalysts. *Catalysis Today*. 1996;**29**:443–447
- [47] Şennik E, Çolak Z, Kılınç N, Öztürk ZZ. Synthesis of highly-ordered TiO₂ nanotubes for a hydrogen sensor. *International Journal of Hydrogen Energy*. 2010;**35**:4420–4427
- [48] Sun XM, Yadong L. Synthesis and characterization of ion-exchangeable titanate nanotubes. *Chemistry - A European Journal*. 2003;**9**:2229–2238
- [49] Varghese OK, Gong D, Paulose M, Ong KG, Grimes CA. Hydrogen sensing using titania nanotubes. *Sensors and Actuators B: Chemical*. 2003;**93**:338–344
- [50] Patterson AL. The Scherrer formula for X-ray particle size determination. *Physical Review*. 1939;**56**:978
- [51] Xing XZ, Jing T, Bin JZ. A Pt-doped TNTA sensor for detecting SF₆ decomposition products. *Sensors*. 2013;**13**:14764–14776
- [52] Xing XZ, Bin JZ, Jia Y, Peng X, Ju T. TiO₂ Nanotube array sensor for detecting the SF₆ decomposition product SO₂. *Sensors*. 2012;**12**:3302–3313